

Ferromagnetic Resonance in Two-dimensional van der Waals Magnets: A Probe for Spin Dynamics

Chunli Tang,¹ Laith Alahmed,¹ Muntasir Mahdi,¹ Yuzan Xiong,² Jerad Inman,² Nathan J. McLaughlin,³ Christoph Zollitsch,⁴ Tae Hee Kim,^{5,6} Chunhui Rita Du,³ Hidekazu Kurebayashi,^{4,7,8} Elton J. G. Santos,^{9,10} Wei Zhang,^{11,2,*} Peng Li,^{12,1,†} and Wencan Jin^{13,1,‡}

¹*Department of Electrical and Computer Engineering, Auburn University, Auburn, AL 36849, USA*

²*Department of Physics, Oakland University, Rochester, MI 48309 USA*

³*Department of Physics, University of California, San Diego, La Jolla, California 92093, USA*

⁴*London Centre for Nanotechnology, University College London, 17-19 Gordon Street, London, WCH1 0AH, UK*

⁵*Center for Quantum Nanoscience, Institute for Basic Science (IBS), Seoul 03760, South Korea*

⁶*Department of Physics, Ewha Womans University, Seoul 03760, South Korea*

⁷*Department of Electronic and Electrical Engineering, University College London, Roberts Building, London, WC1E 7JE, United Kingdom*

⁸*WPI Advanced Institute for Materials Research,*

Tohoku University, 2-1-1, Katahira, Sendai 980-8577, Japan

⁹*Institute for Condensed Matter Physics and Complex Systems,*

School of Physics and Astronomy, The University of Edinburgh, Edinburgh, EH9 3FD, UK

¹⁰*Higgs Centre for Theoretical Physics, The University of Edinburgh, EH9 3FD, UK*

¹¹*Department of Physics and Astronomy, University of North Carolina at Chapel Hill, NC 27599, USA*

¹²*School of Microelectronics, University of Science and Technology of China, Hefei 230052, China*

¹³*Department of Physics, Auburn University, Auburn, AL 36849, USA*

(Dated: January 25, 2023)

The discovery of atomic monolayer magnetic materials has stimulated intense research activities in the two-dimensional (2D) van der Waals (vdW) materials community. The field is growing rapidly and there has been a large class of 2D vdW magnetic compounds with unique properties, which provides an ideal platform to study magnetism in the atomically thin limit. In parallel, based on tunneling magnetoresistance and magneto-optical effect in 2D vdW magnets and their heterostructures, emerging concepts of spintronic and optoelectronic applications such as spin tunnel field-effect transistors and spin-filtering devices are explored. While the magnetic ground state has been extensively investigated, reliable characterization and control of spin dynamics play a crucial role in designing ultrafast spintronic devices. Ferromagnetic resonance (FMR) allows direct measurements of magnetic excitations, which provides insight into the key parameters of magnetic properties such as exchange interaction, magnetic anisotropy, gyromagnetic ratio, spin-orbit coupling, damping rate, and domain structure. In this review article, we present an overview of the essential progress in probing spin dynamics of 2D vdW magnets using FMR techniques. Given the dynamic nature of this field, we focus mainly on the broadband FMR, optical FMR, and spin-torque FMR, and their applications in studying prototypical 2D vdW magnets including CrX_3 ($X = \text{Cl, Br, I}$), Fe_5GeTe_2 , and $\text{Cr}_2\text{Ge}_2\text{Te}_6$. We conclude with the recent advances in laboratory- and synchrotron-based FMR techniques and their opportunities to broaden the horizon of research pathways into atomically thin magnets.

Keywords: Ferromagnetic resonance, magnetization dynamics, spin wave, two-dimensional magnetism, van der Waals materials, spintronics

* zhwei@unc.edu

† lipeng18@ustc.edu.cn

‡ wjin@auburn.edu

Contents

1. Introduction	2
2. Magnetization dynamics and ferromagnetic resonance	3
2.1. Equation of motion and resonance condition	3
2.2. Principle of ferromagnetic resonance	4
3. Broadband FMR	5
3.1. Magnetic anisotropy in chromium trihalides	6
3.2. Anisotropic g -factor	7
3.3. Multidomain structure in chromium trihalides	9
3.4. Weak interlayer antiferromagnetic coupling in chromium trihalides	10
4. Optical FMR	11
4.1. Pump-induced magnetization dynamics	12
4.2. Exciton-magnon coupling	14
5. Spin-Torque FMR	15
6. Conclusion and Perspective	18
6.1. Magneto-optical detection of phase-resolved ferromagnetic resonance	18
6.2. Magnon-photon coupling probed in a superconducting resonator	19
6.3. Nitrogen-vacancy electron spin resonance	21
6.4. Other technical advances	22
7. Acknowledgements	23
References	24

1. Introduction

The demonstration of magnetism in the two-dimensional (2D) limit has long been the focus of fundamental questions in condensed matter physics [1]. In the 1960s, quasi-2D magnetic order has been identified in bulk magnets in which the weak interlayer interactions prevent magnetic ordering in the third dimension [2–4]. In the 1970s, ultrathin film magnetism was realized in elemental metals or metallic alloys thanks to the development of vacuum-deposition techniques [5–7]. Along with the fundamental research of quasi-2D magnets and magnetic thin films, a wide variety of spintronic functionality such as magnetic tunnel junctions and giant magnetoresistance [8–14] has been exploited in data storage and random-access memory applications. In 2017, intrinsic 2D magnetic order was discovered in van der Waals (vdW) crystals $\text{Cr}_2\text{Ge}_2\text{Te}_6$ [15] and CrI_3 [16] when they are exfoliated down to atomically thin flakes. The success of this approach highlights that the intrinsic character of short-range interactions in finite systems can overcome thermal fluctuations and stabilize long-range magnetic order in the 2D limit [17]. Stimulated by this discovery, a rich collection of vdW magnetic materials covering a wide spectrum of magnetic properties are experimental demonstrated using exfoliation, chemical vapor deposition (CVD), and molecular beam epitaxy (MBE) methods, including binary transition metal halides (VI_3 [18], CrCl_3 [19], CrBr_3 [20]), binary transition metal chalcogenides (CrTe_2 [21–23], VSe_2 [24], VTe_2 and NbTe_2 [25], Cr_3X_4 ($\text{X} = \text{S}, \text{Se}, \text{Te}$) [26]), ternary transition metal compounds (MPS_3 or MPSe_3 ($\text{M} = \text{Mn}, \text{Fe}, \text{Ni}$) [27], Fe_nGeTe_2 ($n = 3, 4, 5$) [28–31], MnBi_2Te_4 [32], CrSBr [33], CrSiTe_3 [34]), and other binary transition metal compounds (MnSe_x [35], CrB_2 [36]). For a more extended summary of currently known 2D vdW magnets and their synthesis methods, several recent review articles focused on the material landscape are available [37–40].

As the library of 2D magnets has been rapidly growing over the past few years, there are a couple of important research thrusts that attracted great attention in the field of materials science, microscopic theory, and device applications. First, a large variety of vdW magnets are available and many of their 2D form have not been investigated yet. The magnetic states in 2D materials are distinct from those in bulk crystals. For example, CrI_3 in few-layer form develops layered antiferromagnetic (AFM) configuration below the magnetic onset of 45 K [16], while bulk CrI_3 exhibits a ferromagnetic (FM) order below the Curie temperature of 61 K [41]. The layered AFM states give rise to giant tunneling magnetoresistance, which can be considered as a perfect spin filter [42–45]. The layered AFM states can be

switched to FM states upon applying a moderate magnetic field [16], or electric field [46, 47], or electrostatic doping [48], or hydrostatic pressure [49, 50], opening the route for the development of tunneling-based memory and sensing devices. Therefore, it is instructive to find more 2D semiconducting magnets with layered AFM configuration and to check whether the intimate coupling between spin configuration, electronic state, and stacking symmetry can exist in different compounds as it does in CrI_3 . In addition, to realize industrial applications, the synthesis of 2D magnets with high transition temperature using wafer-scale methods is still pressingly in need. Second, to gain fundamental insights into the 2D magnetic order, it is crucial to understand the microscopic parameters such as dipolar interactions and magnetocrystalline anisotropy. Although the strength of these interactions is typically small, they will have a crucial impact on the 2D vdW magnets. Based on Mermin-Wagner theorem, long-range ferromagnetic or antiferromagnetic order cannot exist in 2D systems at finite temperature for the isotropic Heisenberg model. The main reason for the survival of 2D magnetism is magnetic anisotropy. Third, in addition to the ground state, magnetic excitations provide a basic ingredient of the microscopic description of many physical properties. For example, magnons or spin waves are collective excitations of the spins in magnetically ordered systems. In the 2D isotropic Heisenberg model, the gapless magnon dispersion near the Brillouin zone center leads to the divergence of magnon and the collapse of spin ordering at finite temperature. In contrast, magnetic anisotropy induces a magnon excitation gap, which lifts the Mermin-Wagner restriction and results in finite Curie temperature. Moreover, magnetic excitations play a key role in determining the spin pumping efficiency and switching speed of many spintronic devices. The recent progress of the field of 2D magnets has been extensively reviewed in the literature [38, 40, 51–59].

Despite the new opportunities presented by 2D magnetism, the experimental techniques used to study 2D magnets are still less mature than those used for the well-established bulk magnets and magnetic thin films. Since 2D vdW magnets are typically produced as micrometer-scale thin flakes, macroscopic volumetric analysis tools such as superconducting quantum interference devices (SQUID) magnetometry and neutron scattering are generally not applicable. Optical spectroscopy and microscopy such as polarized micro-Raman scattering [60–70], magneto-optical Kerr effect (MOKE) [16, 46] and magnetic circular dichroism (MCD) [47, 71] have been widely used to study magnetic order parameters of 2D magnets. However, these techniques are highly sensitive to the wavelength of light and the choice of substrate since the magneto-optical response, as shown in CrI_3 and CrBr_3 , is dominated by excitonic effect [72–74].

Ferromagnetic resonance (FMR) has been broadly applied to a range of materials from bulk magnets to nano-scale magnetic thin films. There are several excellent reviews on this technique [75–80]. Nowadays, the unique capabilities of FMR have been exploited to study 2D magnets. First, standard FMR theory shows that the resonance frequency is a function of the effective field, which comprises the information of the exchange coupling, magneto-crystalline and shape anisotropy [81–83]. This dependence can be used to characterize the microscopic parameters of 2D magnets. In addition, the dynamic properties of 2D magnets can be easily perturbed by microwave absorption. Therefore, FMR can be used to explore magnetization dynamics due to varying mechanisms including spin pumping, spin torque, and spin Hall effect. Moreover, analysis of FMR line shape provides direct access to the damping constant, which is the most important parameter for controlling dynamic behaviors in spintronic devices.

In this review, we summarize the recent development of FMR studies of 2D vdW magnet. The article is arranged into sections as follows. Section 1 introduces magnetization dynamics and standard FMR theory using the formalism of Landau–Lifshitz–Gilbert equation. Section 2 shows an experimental setup of broadband FMR that has been implemented in studying the magnetic anisotropy, g -factor, interlayer coupling, and domain structure in the prototypical 2D vdW magnets CrX_3 ($X = \text{Cl}, \text{Br}, \text{I}$) and Fe_5GeTe_2 . Section 3 discusses the optical FMR and the usage of this technique in studying laser-induced magnetization dynamics in $\text{Cr}_2\text{Ge}_2\text{Te}_6$ and CrX_3 , and the magnon-exciton coupling in CrSBr . Section 4 presents the recent advance in spin-torque FMR and highlights its application in 2D-magnets-based spin-orbit torque devices. Finally, we discuss the recent technical advances, future perspectives and challenges in this field.

2. Magnetization dynamics and ferromagnetic resonance

2.1. Equation of motion and resonance condition

Magnetization dynamics cover a wide range of phenomena such as magnetization switching, domain wall motion, and emergence of magnetic textures (vortices, skyrmions and merons). Here, we consider the precessional magnetization dynamics shown in Fig. 1a, in which the motion of magnetic moment around its equilibrium position is described by the phenomenological Landau-Lifshitz-Gilbert (LLG) equation [84, 85]:

$$\frac{d\mathbf{M}}{dt} = -\gamma \mathbf{M} \times \mathbf{H}_{\text{eff}} + \alpha \mathbf{M} \times \frac{d\mathbf{M}}{dt} \quad (1)$$

where \mathbf{M} is the magnetic moment, \mathbf{H}_{eff} is the effective field including the external applied DC field, demagnetization

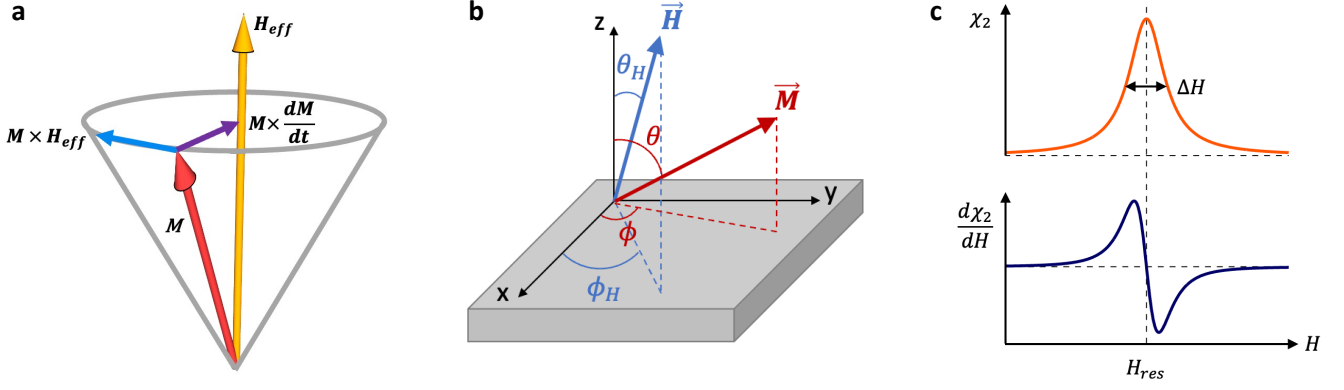


FIG. 1. **a.** The magnetization M (red arrow) precesses about the effective field H_{eff} (yellow arrow). The field-like torque $M \times H_{\text{eff}}$ and damping-like torque $M \times \frac{dM}{dt}$ are shown in blue and purple arrow, respectively. **b.** Coordinate system used to describe the experimental configuration. The orientation of the applied DC magnetic field (\vec{H}) is denoted by (θ_H, ϕ_H) , and the resulting equilibrium orientation of the magnetization (\vec{M}) is given by (θ, ϕ) in spherical coordinates. **c.** Imaginary part of the magnetic susceptibility (χ_2 , orange) as a function of magnetic field (H) and corresponding magnetic field derivative ($d\chi_2/dH$, blue). H_{res} is the resonance field and ΔH is the linewidth.

field, exchange field, and anisotropy field. $\gamma = g\mu_B/\hbar$ is the gyromagnetic ratio, and α is the Gilbert damping parameter. For a free electron $g = 2.0023$, one has $\gamma = 1.7588 \times 10^7$ Hz/Oe. The $M \times H_{\text{eff}}$ term describes the field-like torque that drives the precessional motion of magnetization, while the $M \times \frac{dM}{dt}$ term describes the damping-like torque, which damps the precession and aligns the spin towards the effective field.

Magnetic resonance in ferromagnetic materials at microwave frequencies is similar to nuclear and electron spin resonance. The total magnetic moment precesses around the direction of the effective field (H_{eff}) at the Larmor frequency. The energy of a small transverse microwave field is absorbed when the frequency of the microwave field coincides with the precession frequency. In this case, the precession angle is maximized, and the material will be able to absorb the maximal microwave power. The FMR resonance frequency is dependent on the external magnetic field, magnetic anisotropy, and temperature. This is equivalent to an additional torque exerted on the electron spin, known as the anti-damping-like torque, which acts in the opposite direction of the damping-like torque.

2.2. Principle of ferromagnetic resonance

The details of FMR theory can be found in review articles [77, 78, 80]. Here, the principle of FMR is presented on an intuitive level and the discussion is focused on 2D magnets. Figure 1b shows the typical coordinate system used in FMR experiments, in which (θ, ϕ) and (θ_H, ϕ_H) are the angles for magnetization (\vec{M}) and applied magnetic field (\vec{H}) vector in the spherical coordinates, respectively. As shown in Fig. 1c, the power absorption spectrum is proportional to χ_2 while the field-modulated FMR spectrum is proportional to $d\chi_2/dH$, where χ_2 is the imaginary part of the high-frequency magnetic susceptibility. The field dispersive lineshape [86] is expressed as

$$\frac{d\chi_2}{dH} = A_{\text{sym}} \frac{\Delta H^2}{(H - H_{\text{res}})^2 + \Delta H^2} + A_{\text{asy}} \frac{\Delta H^2(H - \Delta H)}{(H - H_{\text{res}})^2 + \Delta H^2} \quad (2)$$

where H_{res} is the resonance field, ΔH is the linewidth, and A_{sym} and A_{asy} are symmetric and asymmetric Lorentzian components, respectively.

The resonance frequency can be calculated by considering the classical vector of the macroscopic magnetization (M) and the appropriate free energy density (F) in the spherical coordinates defined in Fig. 1b [87, 88]

$$\omega_{\text{res}} = \frac{\gamma}{M \sin \theta} \left[\frac{\partial^2 F}{\partial \theta^2} \frac{\partial^2 F}{\partial \phi^2} - \left(\frac{\partial^2 F}{\partial \theta \partial \phi} \right)^2 \right]^{1/2} \quad (3)$$

where F in an external magnetic field can be evaluated as the sum of exchange interaction, magnetocrystalline anisotropy, magnetoelastic interaction, demagnetization, Zeeman energy, etc.

In general, the magnet moments in 2D vdW magnets originate from the spin and orbital angular momenta of the 3d or 4f electrons in the transition metal ions, which typically interact with the crystal fields associated with crystalline

TABLE I. The anisotropic part of the free energy density (F) for different crystal structures of 2D vdW magnets.

Crystal class	Typical example	2D magnets	Magnetic anisotropy energy
Hexagonal	Co	MX_3 ($M = \text{Cr, V, Ni}$; $X = \text{Cl, Br, I}$), NPS_3 or NPSe_3 ($N = \text{Mn, Fe, Ni}$), $\text{Cr}_2\text{Z}_2\text{Te}_6$ ($Z = \text{Ge, Si}$).	$K_2\sin^2\theta + K_4\sin^4\theta + K_{6\perp}\sin^6\theta + K_{6\parallel}\sin^6\theta\cos^6\phi + \dots$
Trigonal	$\alpha\text{-Fe}_2\text{O}_3$	Fe_3GeTe_2 , MnBi_2Te_4 , 2H-VSe_2 , 1T-VSe_2 .	$K_2\sin^2\theta + K_{41}\sin^4\theta + K_{42}\sin^3\theta\cos\theta\cos^3\phi + K_{61}\sin^6\theta + K_{62}\sin^6\theta\cos^6\phi + K_{63}\sin^3\theta\cos^3\theta\cos^3\phi$
Tetragonal	$\text{Ni,Co,Fe/Cu}(001)$	FeTe	$K_2\sin^2\theta + K_{4\perp}\sin^4\theta + K_{4\parallel}\sin^4\theta\cos^4\phi + \dots$
Orthorhombic	Fe_3O_4	VOX_2 ($X = \text{Cl, Br, I}$)	$\sin^2\theta(K_1\cos^2\phi + K_2\sin^2\phi) + \sin^4\theta(K_3\cos^2\theta + K_4\sin^2\phi\cos^2\phi + K_5\sin^4\phi) + \dots$

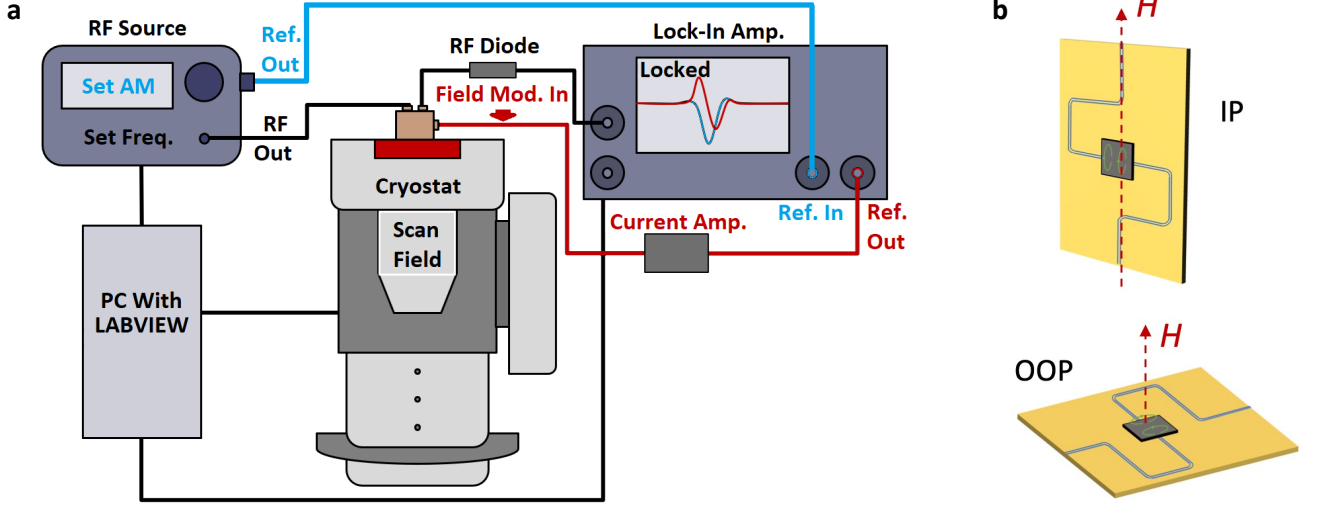


FIG. 2. Broadband FMR spectroscopy setup. **a.** Main components of broadband FMR include a RF source, a cryostat, a RF diode, and a lock-in amplifier. A controllable DC magnetic field is provided by a physical properties measurement system. The amplitude- and field-modulated spectra are shown in blue and red, respectively. **b.** Schematic of a co-planar waveguide with magnetic field applied in the in-plane (IP) and out-of-plane (OOP) geometry, respectively.

symmetries. Therefore, most of the currently known 2D vdW magnets can be classified into hexagonal, trigonal, tetragonal, and orthorhombic lattices. The anisotropic part of the free energy density (F) for these crystal structures is summarized in Table I.

3. Broadband FMR

FMR can be used as a spectroscopy method to gain insight into the magnetization dynamics in magnetic materials. A broadband FMR spectroscopy setup is shown in Fig. 2a, which typically is comprised of the following equipment: a controllable DC magnetic field source, such as a physical properties measurement system (PPMS), a radio-frequency (RF) source to supply the required microwave current, a co-planar waveguide (CPW) to deliver microwaves of different frequencies to the sample, an RF diode to convert the returned microwave current into a detectable voltage. Figure 2b shows the typical measurements performed in the in-plane (IP) and out-of-plane (OOP) configuration when the magnetic field is applied along the vertical direction in a PPMS setup. Due to the high-frequency nature, it is difficult to detect RF signals with an adequate signal-to-noise ratio. Therefore, a low-frequency envelope is added to the RF

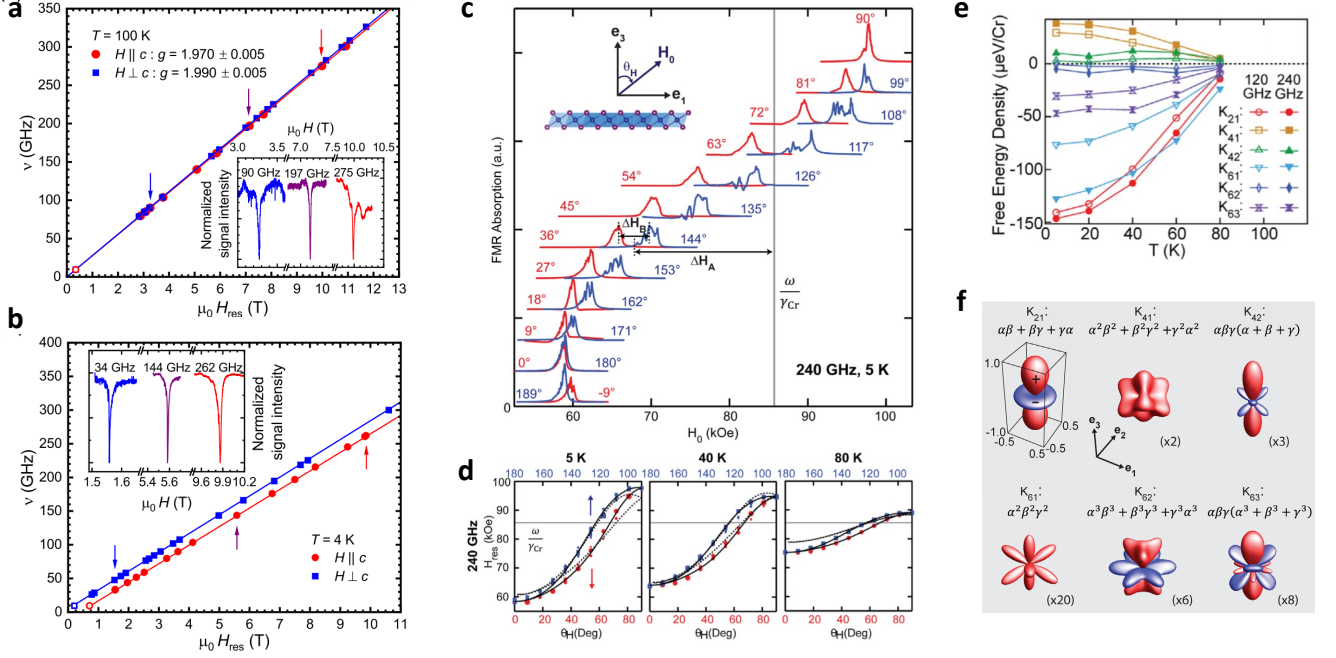


FIG. 3. Frequency dependence of the resonance field H_{res} at **a.** 100 K and **b.** 4 K, respectively. Measurements were carried out with the external magnetic field applied parallel (red circles) and perpendicular (blue squares) to the crystallographic c axis, respectively. **c.** Evolution of the FMR spectra as θ_H is varied, measured at 240 GHz and 5 K. Each spectrum is offset and scaled moderately for clarity. The same offset is applied for θ_H and $180^\circ - \theta_H$. ΔH_A and ΔH_B are two anisotropy features in H_{res} . ω/γ_{Cr} denotes the corresponding H_{res} for a free Cr^{3+} ion spin. **d.** H_{res} vs θ_H for various temperatures. The solid black lines are fits to the free energy function [Eq. (6)]. **e.** Temperature dependence of the coefficients K_{pq} associated with the basic anisotropy structures. **f.** Basic anisotropy structure in terms of the cosines α, β, γ (the projections of the magnetization onto the x, y, z directions). The sizes are rescaled relative to that for $\alpha\beta + \beta\gamma + \gamma\alpha$ with the indicated magnifications. Red (blue) denotes positive (negative) values. Panels **a-b** are adapted from Ref. [89]. Panels **c-f** are adapted from Ref. [90].

signals, which can be measured using a lock-in amplifier. The low-frequency envelope can be added either through the RF source itself if it supports amplitude modulation (AM), which is highlighted in blue in Fig. 2a. It can also be added externally by supplying an AC signal to a set of Helmholtz coils, which can then modulate the RF current passing through it. This field-modulation option is highlighted in red in Fig. 2a.

3.1. Magnetic anisotropy in chromium trihalides

Even though the presence of magnetic anisotropy is not a requisite for the appearance of magnetism in strictly two dimensions as recently demonstrated [17], for device implementation and spintronic applications the characterization of a sizeable magnetic anisotropy becomes a key task. FMR spectroscopy is a valuable tool to accomplish this aim because the shift in the resonance field of a few Oersted's can be easily detected, which corresponds to an energy resolution in the determination of magnetic anisotropy on the order of $0.1 \mu\text{eV}$ [77].

Chromium trihalides (CrX_3 , $X = \text{Cl, Br, I}$) represent a prototypical vdW magnet, in which the Cr^{3+} cations ($3d^3$, $S = 3/2$) form a honeycomb structure with the edge-sharing octahedral coordination formed by six halogen anions [91, 92]. For CrCl_3 , below the magnetic transition temperature ($T_c = 17$ K), spins in the honeycomb layers are coupled ferromagnetically and oriented within the ab plane, while spins in neighboring layers are coupled by a weaker antiferromagnetic interaction [19, 93, 94]. To determine the details of the magnetic anisotropy in CrCl_3 , frequency-dependent FMR investigations were conducted at 100 and 4 K [89]. The resulting frequency-field diagrams are shown in the main panels of Fig. 3a and 3b and exemplary spectra are presented in their insets. At 100 K a linear frequency-field dependence of resonance $\nu(H_{res})$ is observed for both orientations of the external magnetic field. Such behavior is expected in the paramagnetic regime of CrCl_3 and can be well described by the standard resonance condition of a paramagnet

$$\nu = g\mu_B\mu_0 H_{res}/h \quad (4)$$

where g , μ_B , μ_0 and h denote the g -factor, Bohr's magneton, vacuum permeability, and Planck's constant, respectively. Fits to the data according to Eq. (4) yielded a g -factor with merely small deviation from the free-electron g -factor of 2 as well as very slight anisotropy. The result is consistent with the expected value for Cr^{3+} ions and indicates that the magnetism in CrCl_3 is largely dominated by the spin degrees of freedom while the orbital angular momentum is completely quenched. Consequently, the spin-orbit coupling and intrinsic magnetocrystalline anisotropies are very weak (or even negligible) in CrCl_3 , as it was also suggested in the literature [94, 95].

In contrast, the data collected at 4 K (see Fig. 3b), i.e., in the magnetically ordered state, shows a clear anisotropy regarding the two magnetic-field orientations. For $H \perp c$, the resonance positions shift towards smaller magnetic fields for all measured frequencies, while for $H \parallel c$, the resonance positions shift to higher magnetic fields. Qualitatively, such behavior reflects a ferromagnetically ordered system with an easy-plane anisotropy. Quantitatively, the sources of magnetic anisotropy can be evaluated using the free energy density below

$$\begin{aligned} F = & -\mu_0 H \cdot M - K_U \cos^2(\theta) \\ & + \frac{1}{2} \mu_0 M^2 [N_x \sin^2(\theta) \cos^2(\phi) \\ & + N_y \sin^2(\theta) \sin^2(\phi) + N_z \cos^2(\phi)] \end{aligned} \quad (5)$$

where the first term is the Zeeman-energy density describing the coupling between the magnetization vector and the external magnetic field, the second term represents the uniaxial magnetocrystalline anisotropy whose strength is parametrized by the energy density K_U , and the third term is the shape anisotropy energy density which is characterized by the demagnetization factors N_x , N_y , and N_z . An excellent agreement between this model and the measured resonance positions can be accomplished by setting K_U to zero, indicating the magnetic anisotropy is solely due to the shape anisotropy caused by long-range dipole-dipole interactions, whereas the intrinsic magnetocrystalline anisotropy can be neglected. Similar magnetic anisotropy investigation were also performed in the vdW magnet $\text{Cr}_2\text{Ge}_2\text{Te}_6$ [96].

Comparing with CrCl_3 , it was concluded that the magnetic anisotropy in CrI_3 arises from a dominant uniaxial or single-ion anisotropy [97, 98]. However, theoretical proposals and experimental measurements have highlighted the important contributions from high-order exchange interactions (e.g., biquadratic) [99, 100], the off-diagonal term (Γ) and Kitaev interaction (K) in the Heisenberg-Kitaev ($J - K - \Gamma$) Hamiltonian [101–104]. The structure of the magnetic anisotropy in CrI_3 can be obtained from angle-dependent FMR by measuring the change of the resonance field as the direction of the external field (H_0) is varied. Figure 3c shows a representative example of the FMR spectra for different θ_H at 240 GHz and 5 K. Two distinct features are crucial to analyzing the anisotropy: ΔH_A is the shift in H_{res} from the free ion contribution $\omega/\gamma_{\text{Cr}}$, where γ_{Cr} is the gyromagnetic ratio of Cr^{3+} , and ΔH_B is the difference in H_{res} between θ_H and $180^\circ - \theta_H$. Figure 3d shows the resonance field $H_{\text{res}}(\theta_H, \omega, T)$ at varying temperatures. A free energy functional is constructed below to fit the data as shown in the black solid curves in Fig. 3d.

$$\begin{aligned} F = & -\mu_0 H \cdot M + 2\pi M^2 \cos^2(\theta) + K_{21}(\alpha\beta + \beta\gamma + \gamma\alpha) \\ & + K_{41}(\alpha^2\beta^2 + \beta^2\gamma^2 + \gamma^2\alpha^2) + K_{42}\alpha\beta\gamma(\alpha + \beta + \gamma) \\ & + K_{61}\alpha^2\beta^2\gamma^2 + K_{62}(\alpha^3\beta^3 + \beta^3\gamma^3 + \gamma^3\alpha^3) \\ & + K_{63}\alpha\beta\gamma(\alpha^3 + \beta^3 + \gamma^3) \end{aligned} \quad (6)$$

where the first and second term are Zeeman energy and shape anisotropy, respectively. K_{pq} are coefficients associated with the quadrupole interaction. Remarkably, the high spectroscopic precision of FMR enables the evaluation of the μeV -scale quadrupole interaction constants. The extracted values of the K_{pq} and corresponding basic anisotropy structure are shown in Fig. 3e and 3f, respectively. The results show that Kitaev interaction is the strongest in CrI_3 , much larger than the Heisenberg exchange, and responsible for opening the gap at the Dirac points in the spin-wave dispersion [90]. Nevertheless, inelastic neutron scattering experiments [105–107] undertaken on bulk CrI_3 have pointed out to different conclusions on the magnitude of the Kitaev term influencing the formation of the Dirac gap. That is, the most updated values [107] resulted in negligible contributions of the Heisenberg-Kitaev Hamiltonian and electron correlation effects to the spin waves and Dirac spin gap in CrI_3 . The dataset is approximately consistent with a Heisenberg Hamiltonian including anisotropy, exchange interactions and Dzyaloshinskii-Moriya interaction (DMI) with consideration of both the c axis and in-plane DMI. Additional FMR experiments would be needed to fully address this discrepancy.

3.2. Anisotropic g -factor

Understanding the mechanism of ferromagnetism in metals has been a longstanding nontrivial question in a wide variety of condensed-matter systems [109–112]. Along with the rapidly growing interest in searching for novel vdW

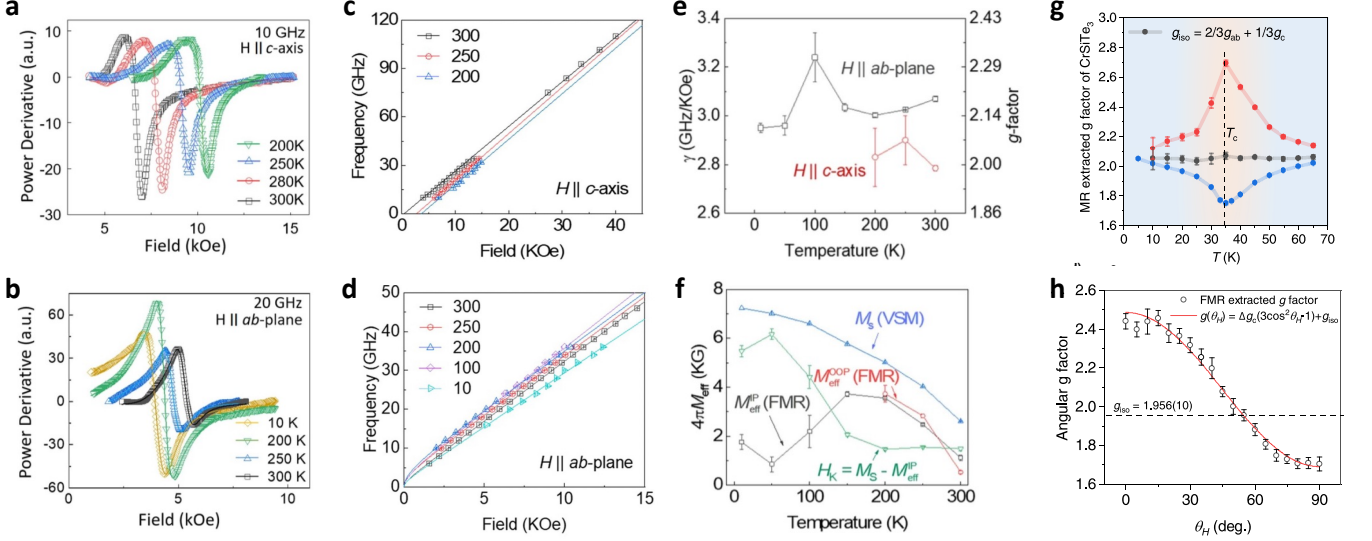


FIG. 4. FMR spectra acquired at varying temperatures for **a.** $H \parallel c$ -axis and **b.** $H \parallel ab$ -plane. The raw data in **a** and **b** are fitted to field-derivative lineshape using Eq. (2). **c.** and **d.** Frequency vs. resonance field at varying temperatures for $H \parallel c$ -axis and $H \parallel ab$ -plane, respectively. The data points are fitted to corresponding Kittel equations. **e.** Temperature dependence of the gyromagnetic ratio γ and spectroscopic g -factor for the $H \parallel c$ (red) and $H \parallel ab$ (black) cases, respectively. **f.** Temperature dependence of saturation magnetization $4\pi M_s$ and effective magnetization $4\pi M_{\text{eff}}$ from VSM and FMR measurements, respectively. **g.** Comparison of the temperature-dependent g -factor extracted from FMR data above saturation field. Calculation of isotropic component $g_{\text{iso}} = 2/3g_{ab} + 1/3g_c$ is basically in line with the spin-only value $g = 2$. **h.** Angular dependence of the extracted g -factor. The red line is fitted by $g(\theta_H) = \Delta g(3\cos^2\theta_H - 1) + g_{\text{iso}}$. Panels **a-f** are adapted from Ref. [108]. Panels **g-h** are adapted from Ref. [34].

magnets, one particular issue has been clarifying whether an orbital with magnetic moment should be considered in a localized or itinerant picture because long-range magnetism starting from localized isotropic Heisenberg spins is not allowed in two dimensions. Fe_nGeTe_2 ($n = 3, 4, 5$) represent a class of metallic vdW ferromagnets with high Curie temperature [28, 30, 113, 114]. Among them, Fe_5GeTe_2 has a complex atomic structure with multiple nonequivalent iron sites [113, 115, 116]. Recent theoretical calculations have shown that the orbital states associated with the nonequivalent iron sites have distinct impact on the magnetic ground state [117]. In addition, x-ray magnetic circular dichroism studies of elemental selective valence-band electronic and spin states highlight significant ligand states (Ge $4p$ and Te $5p$) contribution to the ferromagnetism through hybridization with the Fe $3d$ orbital [118].

The mixture of orbital momentum and magnetic moment causes the shift of g -factor from the free electron value, which may be different along different crystallographic directions, that is, one has to consider a g -tensor. This can be demonstrated by writing the magnetic moment $M = -\mu_B(L + 2S) \rightarrow g\mu_B S'$, where S' is an effective spin. The contribution of orbital momentum contained in the g -tensor can be obtained by direct measurements of g -factor using FMR spectroscopy. In the best cases, g -factors of metallic ferromagnets are usually quoted with an error bar of 1% [77].

FMR spectroscopy studies of the magnetization dynamics of Fe_5GeTe_2 are summarized in Fig. 4a-4f [108]. The FMR spectra for the $H \parallel c$ -axis and $H \parallel ab$ -plane at selected temperatures are shown in Fig. 4a and 4b, respectively. The profiles were fitted to the field-derivative lineshape using Eq. (2) to extract the resonance fields. The microwave frequencies (f) as a function of extracted resonance fields (H_{res}) were plotted in Fig. 4c and 4d. The gyromagnetic ratio (γ) and corresponding g -factor, along with the effective magnetization $4\pi M_{\text{eff}}$ can be obtained by fitting the f vs. H_{res} data to the Kittel equations as follows:

$$\begin{aligned} H \parallel c: \quad f_{\text{OOP}} &= \frac{\gamma}{2\pi} (H_{\text{res}} - 4\pi M_{\text{eff}}) \\ H \parallel ab: \quad f_{\text{IP}} &= \frac{\gamma}{2\pi} \sqrt{(H_{\text{res}} + 4\pi M_{\text{eff}})H_{\text{res}}} \end{aligned} \quad (7)$$

The gyromagnetic ratio and corresponding g -factor for both field orientations are shown in Fig. 4e, revealing an anisotropic g -factor that, in both cases, deviates from $g = 2$. The anisotropic g -factor can be interpreted physically: a small orbital moment arising from reduced crystalline symmetry may lock the large isotropic spin moment into its favorable lattice orientation through spin-orbit coupling, giving rise to a sizable magnetic anisotropy. Therefore, it is

likely that the orbital moment is closely linked to the magnetocrystalline anisotropy in itinerant ferromagnets.

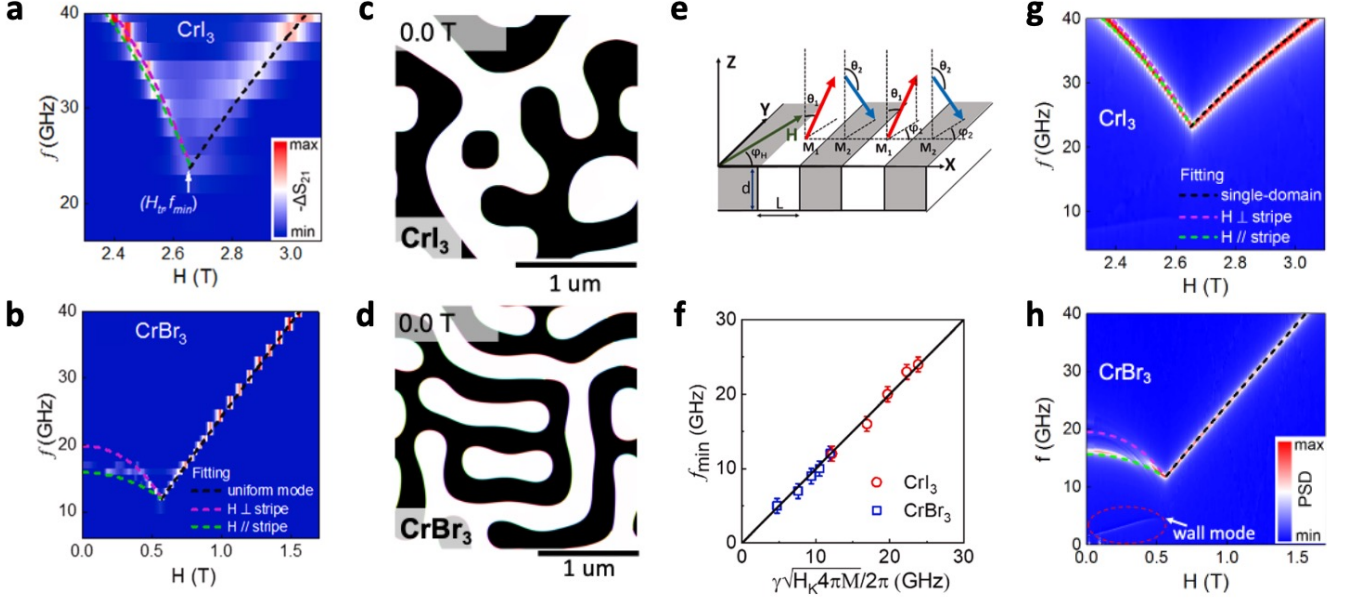


FIG. 5. The color map of FMR spectra at 10 K for **a.** CrI₃ and **b.** CrBr₃. The dash lines are fitting curves of the uniform mode (black) and the calculated curves using multi-domain FMR theory (red and green). The simulated domain structures at 10 K and zero field for **c.** CrI₃ and **d.** CrBr₃. **e.** The illustration of magnetization structures for the stripe domain phase with the in-plane field for the multi-domain FMR calculation. **f.** The correlation between the experimental values of f_{\min} and $\gamma/2\pi\sqrt{H_K \cdot 4\pi M}$. The solid line is calculated by Eq. (11). The color map of simulated FMR spectra utilizing the magnetic parameters for **g.** CrI₃ and **h.** CrBr₃ at 10 K. All panels are adapted from Ref. [119].

It is worth noting that an unsaturated magnetization at FMR can also lead to an inaccurate estimation of the gyromagnetic ratio. The FMR-extracted effective magnetization, which includes the saturation magnetization as well as the magnetocrystalline anisotropy field H_K can be comparable with the saturation magnetization extracted from the VSM measurements, as shown in Fig. 4f. To confirm the g -factor anisotropy, FMR measurements at high-frequency and high-magnetic-field are needed.

Beyond the spin-orbit coupling-induced g -factor shift at zero field, the Nagata theory [120, 121] indicates that a correction of g -factor shift under high-temperature perturbation approximation and in the presence of finite magnetic field should be considered for the studies of critical phenomena in low-dimensional magnet. Recently, temperature dependence of g -factor in ferromagnetic semiconductor CrSiTe₃ has been investigated using broadband three-dimensional vector-ferromagnetic resonance experiments [34]. As shown in Fig. 4g, the clear downwards- or upwards shifts of the g -factor, with a maximum value at $T_c = 34.15$ K, are observed at varied temperature. The shift of g -factor near the critical temperature is attributed to the enhanced magnetic fluctuations and anisotropic exchange interactions. In addition, the cryogenic vector magnet system allows angular dependent measurements of g -factor at T_c . As shown in Fig. 4h, the $(3\cos^2\theta_H - 1)$ like angular dependence derived from the Nagata theory fits well with the FMR extracted g -factor, where the magic angle with a spin-only g -factor is observed at $\theta_H = 54.74^\circ$.

3.3. Multidomain structure in chromium trihalides

The broadband FMR experiments can be combined with micromagnetic and atomistic simulations to investigate the magnetic properties of vdW magnets associated with domain structures. In complement to the microscopy techniques such as Lorentz transmission electron microscopy and magneto-optical microscopy, FMR results emphasize on the dynamical properties which provide essential information for device applications such as magnetic switching, magnon excitation, and damping mechanism. An exemplary work is an FMR measurement of magnetization dynamics of CrI₃ and CrBr₃ crystals in a broad frequency range of 1 – 40 GHz and over a wide temperature range of 10 – 300 K [119].

The color maps in Fig. 5a (CrI₃) and 5b (CrBr₃) show that the resonance frequency first decreases with H towards a critic field H_{tr} , then increases with H at higher field, giving rise to a minimum resonance frequency f_{\min} at H_{tr} . A quantitative analysis of the FMR features is based on the periodic stripe domain structure which can

be reproduced via micromagnetic (see Fig. 5c and 5d) and atomistic simulations[99, 122]. The sample consists of two sets of domains with equal volume, and the magnetization in the neighboring domain should have the opposite magnetization component along z -direction, thus there is no net M_z under the in-plane magnetic field. The free energy density for the multi-domain structure can be written as

$$\begin{aligned}
 F = & -\frac{H \cdot M}{2}(\sin\theta_1 \sin\phi_1 + \sin\theta_2 \sin\phi_2) \\
 & + \frac{K_z}{2}(\sin^2\theta_1 + \sin^2\theta_2) + \frac{4\pi}{2} \frac{M^2}{4}(\cos\theta_1 + \cos\theta_2)^2 \\
 & + \frac{N_x}{2} \frac{M^2}{4}(\sin\theta_1 \cos\phi_1 - \sin\theta_2 \cos\phi_2)^2 \\
 & + \frac{N_y}{2} \frac{M^2}{4}(\sin\theta_1 \sin\phi_1 - \sin\theta_2 \sin\phi_2)^2 \\
 & + \frac{N_z}{2} \frac{M^2}{4}(\cos\theta_1 - \cos\theta_2)^2
 \end{aligned} \tag{8}$$

where M represents the saturation magnetization of material, θ_1 and θ_2 represent the out-of-plane angles of domain magnetization, ϕ_1 and ϕ_2 represent the in-plane projection angles of magnetization in each domain, K_z is the perpendicular magnetic anisotropy energy density. (N_x, N_y, N_z) are the demagnetization parameters of each domain with the relation of $N_x + N_y + N_z = 4\pi$. Figure 5e shows that the domain system follows the conditions of $\theta_1 + \theta_2 = \pi$ and $\phi_1 = \phi_2 = \phi_H$. The resonance frequency f in the multi-domain state depends on the in-plane field angle ϕ_H . For $\phi_H = 0^\circ$ with $H \perp$ strip, the FMR frequency can be described by

$$f = \frac{\gamma}{2\pi} \sqrt{H(H - H_K + 4\pi M)} \tag{9}$$

and for $\phi_H = 90^\circ$ with $H \parallel$ strip, the FMR frequency can be described by

$$f = \frac{\gamma}{2\pi} \sqrt{H_K^2 + 4\pi M \cdot H^2 / H_K - H^2} \tag{10}$$

The relative angle ϕ_H between the stripe domain and the applied field could vary between 0° and 90° , then the corresponding FMR frequency should vary between the values calculated by Eq. (9) and Eq. (10). As a result, the minimum FMR frequency f_{\min} is obtained when the field H_{tr} equal to H_K

$$f = \frac{\gamma}{2\pi} \sqrt{H_K \cdot 4\pi M} \tag{11}$$

Thus, f_{\min} can be calculated by Eq. (11) with experimentally determined γ , H_K , and $4\pi M$, as shown in Fig. 5f. Starting from the labyrinth domain structure at 10 K and zero field, field-dependent evolution of domain structures can be simulated by gradually applying the in-plane field along x -axis. The color maps (Fig. 5g and 5h) generated from the simulation agree with the experimental results (Fig. 5a and 5b) very well. Similar color maps of frequency-dependent ferromagnetic resonance spectra and multi-domain structure have also been demonstrated in $\text{Cr}_2\text{Ge}_2\text{Te}_6$ [96].

3.4. Weak interlayer antiferromagnetic coupling in chromium trihalides

CrI_3 and CrCl_3 have been shown to be layered antiferromagnetic insulators in their few-layer form, in which spins within each layer have a ferromagnetic nearest-neighbor coupling, whereas spins in adjacent layers have a weak antiferromagnetic coupling [16, 19, 124, 125]. Because of the weak interlayer antiferromagnetic coupling in CrCl_3 is within the typical microwave range, it allows to excite both acoustic and optical modes (see Fig. 6a) [123]. Magnetic resonance measurements were carried out by fixing the excitation frequency and sweeping the applied magnetic field (see experimental geometry in Fig. 6b). Only one resonance is observed when the DC magnetic field is applied perpendicular to the RF field (H_\perp , see Fig. 6d), but two resonances show up when the DC magnetic field is applied parallel to the RF field (H_\parallel , see Fig. 6c). The optical mode and acoustic mode are centered around the frequencies ω_\pm with magnetic field dependence as follows:

$$\begin{aligned}
 \omega_+ &= \mu_0 \gamma \sqrt{2H_E M_s \left(1 - \frac{H^2}{4H_E^2}\right)} \\
 \omega_- &= \mu_0 \gamma \sqrt{2H_E (2H_E + M_s)} \left(\frac{H}{2H_E}\right)
 \end{aligned} \tag{12}$$

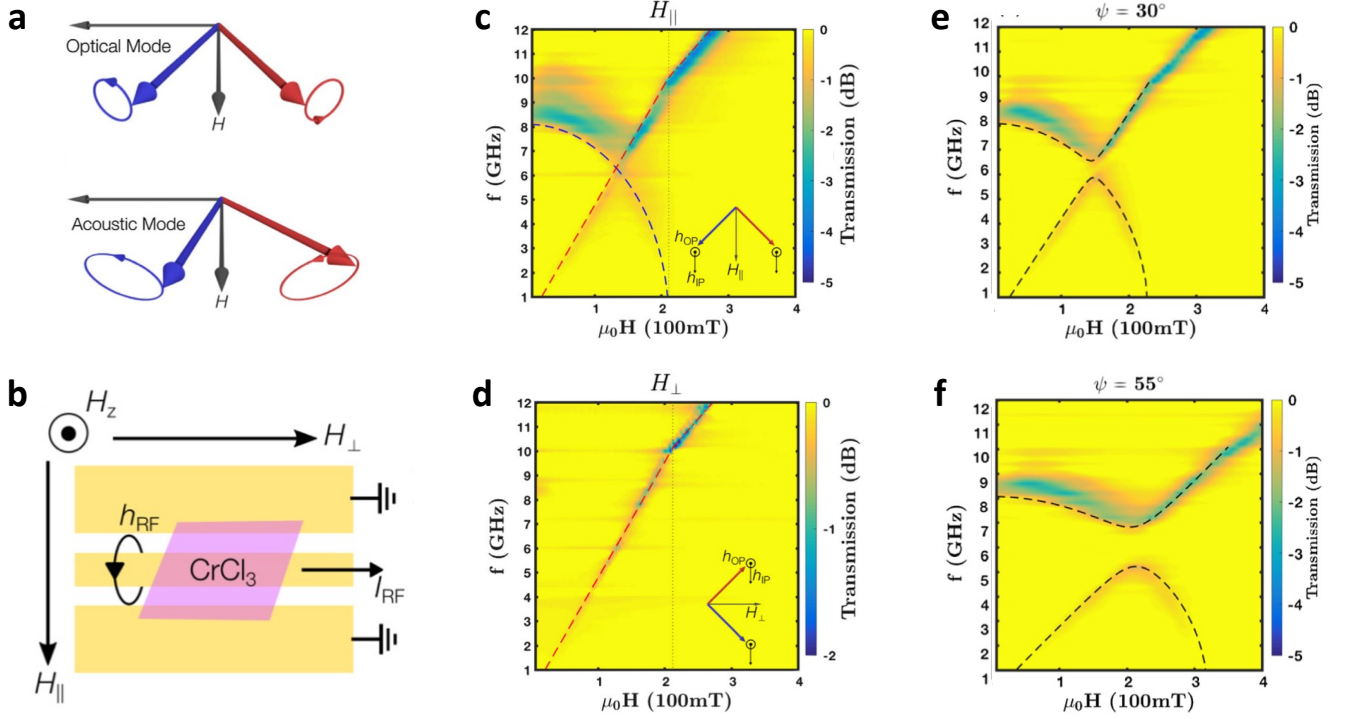


FIG. 6. **a.** Schematic of the precession orbits for the two sublattice magnetizations in the optical mode and the acoustic mode. **b.** Experimental schematic featuring a coplanar waveguide with a CrCl₃ crystal placed over the signal line. H_{\parallel} , H_{\perp} , and H_z are the components of the applied DC magnetic field. Microwave transmission as a function of frequency and in-plane magnetic field at 1.56 K with the magnetic field applied **c.** parallel and **d.** perpendicular to the in-plane RF field. Two modes are observed in the H_{\parallel} configuration: an optical mode that has finite frequency at zero applied field, and an acoustic mode with frequency proportional to the applied field. Only the acoustic mode is observed in the H_{\perp} configuration. Out-of-plane field applied at an angle of **e.** $\psi = 30^\circ$ and **f.** $\psi = 55^\circ$ breaks the symmetry and couples the two modes resulting in tunable gaps. All panels are adapted from Ref. [123].

where H_E is the interlayer exchange field and M_s is the saturation magnetization. The two modes in Fig. 6a can be fitted to Eq. (12), which are shown by the dashed lines in Fig. 6c with fit parameters of $\mu_0 H_E = 105$ mT and $\mu_0 M_s = 396$ mT at $T = 1.56$ K. Note that the acoustic mode changes its slope at $\mu_0 H \approx 200$ mT. This occurs because the moments of the two sublattices are aligned with the applied field when $H > 2H_E$. In this case the crystal behaves as a ferromagnet and the acoustic mode transforms into uniform ferromagnetic resonance described by the Kittel formula.

When the magnetic field is applied in plane, the system is symmetric under two-fold rotation around the applied field direction combined with sublattice exchange. This prevents hybridization between the optical and acoustic modes, leading to a degeneracy where they cross. To break the rotational symmetry, a magnetic field can be applied at a range of angles, ψ , from the coplanar waveguide. For $\psi = 30^\circ$, a gap opens near the crossing point (see Fig. 6e). Increasing the tilt angle ($\psi = 55^\circ$) increases the gap size as shown in Fig. 6f until the mode coupling becomes zero again when ψ approaches 90° . The strong magnon-magnon coupling in CrCl₃ with large tunable gap up to 1.37 GHz may hold promise of potential applications in hybrid quantum systems.

4. Optical FMR

Ferromagnetic resonance can also be detected using a set of established optical techniques including magneto-optical Faraday effect, magneto-optical Kerr effect, and transient reflectivity. Optical detection of FMR is typically performed by pump-probe experiments [126–130], which usually consists of ultrafast lasers, well-aligned opto-mechanical delay-line, high-level vibration control, and balanced detection (see Fig. 7a) [131, 132]. As shown in the insets of Fig. 7b, the changes in the sample's magnetization can be correlated to the Faraday/Kerr rotation angle via magneto-optical effect, which is dominated by the thermalization processes between different energy carriers, namely, electrons, phonons, and magnons. The Faraday/Kerr signals contain damped oscillating fringes resulting from spin precession,

which allows for the analysis of the spin wave modes and damping constant of magnetic materials.

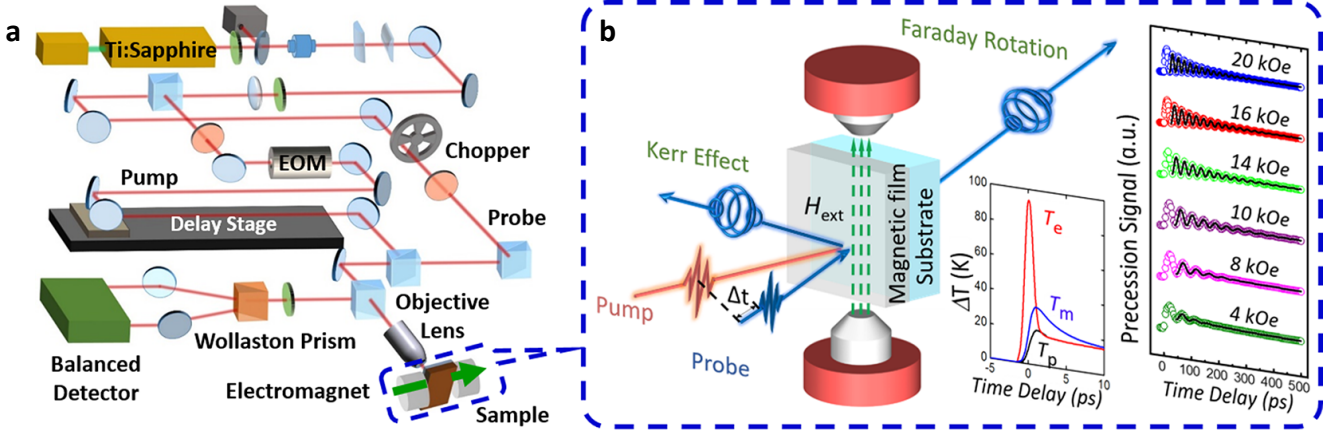


FIG. 7. **a.** Layout of an example optical FMR setup. A mode-locked Ti:sapphire laser produces a train of pulses with a duration of ~ 100 fs and a center wavelength of ~ 800 nm. A polarizing beam splitter separates the laser into pump and probe beams with orthogonal polarizations. The pump beam is modulated as a sinusoidal wave by an electro-optical modulator (EOM). A mechanical delay stage varies the optical path of the pump beam, producing a time separation between the pump excitation and probe sensing. The probe beam is split into two paths of orthogonal polarizations by a Wollaston prism and the changes in the relative intensities of these two probe paths are detected by a balanced detector, which is related to the variations in the polarization states. **b.** Mechanism of spin dynamics with optical excitation. Both the Faraday rotation (transmission) and the Kerr rotation (reflection) are illustrated, depending on the measurement configuration. Insets show the phenomenological three-temperature model that considers energy exchange between electrons (T_e), phonons (T_p), and magnons (T_m), and the typical pump-probe signal as a function of delay time acquired under varying magnetic fields. All panels are adapted from Ref. [132]

4.1. Pump-induced magnetization dynamics

Recently, magnetization dynamics in $\text{Cr}_2\text{Ge}_2\text{Te}_6$ nanoflakes have been studied by means of a two-color time-resolved Faraday rotation with a picosecond time resolution at cryogenic temperature [133]. Below the Curie temperature, a pump beam of femtosecond pulses intensively heats the ferromagnet to produce instantaneous demagnetization and trigger the magnetization precession. By monitoring pump-induced magnetization dynamics in an external magnetic field H_{ext} , the angular dependence of the precession frequency and the transverse spin relaxation time can be determined.

Figure 8a plots the pump-induced magnetization dynamics up to 1500 ps for $\theta_H = 50^\circ$ at three external fields $H_{\text{ext}} = 211, 418,$ and 680 mT. The time resolution of the pump-probe measurements is estimated to be 1.2 ± 0.01 ps (see inset of Fig. 8a). This ultrafast process can be qualitatively understood by considering a drastic increase in the spin temperature leading to a reduction of both the magnetization M and the effective magnetic field H_{eff} . After spin cooling of a few picoseconds, M recovers its magnetization saturation value while the electron temperature cools through phonon emission. The change of magnetization as a function of time delay $\Delta M(\Delta t)$ probed by the Faraday rotation can be phenomenally described as

$$\Delta M(\Delta t) \sim A_0 e^{-\delta t / \tau_T} \cos(2\pi f \Delta t + \phi_0) + A_1 e^{-\delta t / \tau_{p1}} + A_2 e^{-\delta t / \tau_{p2}} \quad (13)$$

Here, the first term describes the spin-precession dynamics in which A_0 , τ_T , f , and ϕ_0 denote the magnetization amplitude, the transverse spin relaxation time, the precession frequency, and the initial phase, respectively. The second and third terms describe the magnetization recovery process, where A_1 (A_2) and τ_{p1} (τ_{p2}) are, respectively, the demagnetization magnitude and the characteristic time constant of a short (long) process. By fitting the experimental data to Eq. (13), one can obtain the precession frequency, oscillation magnitudes, and magnetization recovery-time. The frequency f and the transverse spin relaxation rate τ_T^{-1} as a function of the external magnetic field are shown in Fig. 8c and 8d. All the f vs H_{res} can be fitted to a Kittel equation, yielding $\mu_0 H_K = 125 \pm 8$ mT and a g -factor of 2.04 ± 0.03 . The magnetization recovery-time constants $\tau_{p1} \approx 400 \pm 150$ ps and $\tau_{p2} \approx 8 \pm 2$ ns, which are similar

for different H_{ext} . The two relaxation processes are quite likely related to energy relaxation by optical and acoustic phonons in semiconductor structures at low temperatures.

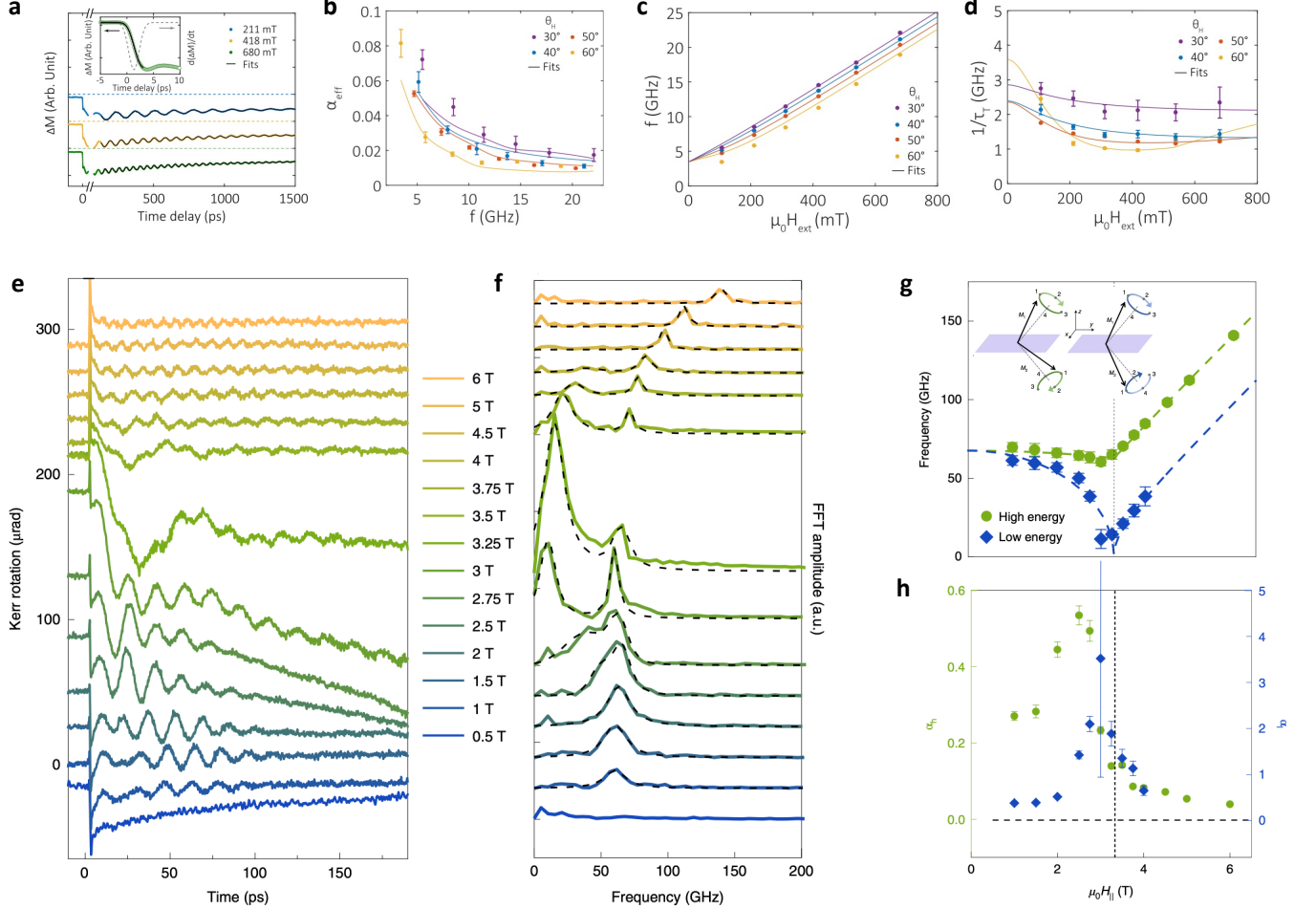


FIG. 8. **a**. Normalized magnetization dynamics due to laser heating in $\text{Cr}_2\text{Ge}_2\text{Te}_6$ for selected H_{ext} (211, 418, and 680 mT) at $\theta_H = 50^\circ$. Solid lines are fits to Eq. (13) and dashed lines are baselines in the absence of pumping. Inset: Magnetization dynamics (markers) and cumulative Gauss fit (line) in the first 10 ps (left axis). Dashed line (right axis) is the differential curve of the fit, which gives a time resolution of 1.2 ± 0.01 ps. **b**. Effective damping α_{eff} calculated from τ_T , H_1 , and H_2 vs precession frequency f at varied θ_H (markers). Solid lines are fits to Eq. (14). **c**. Precession frequency (f) and **d**. transverse spin relaxation rate (τ_T^{-1}) as a function of H_{ext} at changing θ_H of 30° , 40° , 50° , and 60° . Markers denote experimental data and solid lines are fitted to the Kittel equation. **e**. Kerr rotation as a function of pump-probe delay time in bilayer CrI_3 under different in-plane magnetic fields and **f**. corresponding fast Fourier transform (FFT) spectra after the removal of the demagnetization dynamics (exponential decay). The curves are vertically displaced for clarity. **g**. Frequency and **h**. damping rates of high energy (ω_h) and low energy (ω_l) modes as a function of in-plane magnetic field. Dashed lines in **g** and **h** are fits to the LLG equation. Inset of **g** shows the spin precession eigenmodes of ω_h and ω_l under an in-plane field (y axis). The vertical dotted lines in **g** and **h** indicate the in-plane saturation field from the fits to the LLG equation. Panels **a-d** are adapted from Ref. [133]. Panels **e-h** are adapted from Ref. [134].

Moreover, by combining the LLG equation and the Kittel formula, the effective damping coefficient α_{eff} is given by the relation

$$\alpha_{\text{eff}} = \frac{2}{\gamma\tau_T(H_1 + H_2)} \quad (14)$$

Figure 8b shows α_{eff} as a function of frequency f , which is obtained by using τ_T and deviation of magnetization from the easy axis (θ_M) to determine $H_1 = H_{\text{ext}}\cos(\theta_M - \theta_H) + H_K\cos^2\theta_M$ and $H_2 = H_{\text{res}}\cos(\theta_M - \theta_H) + H_K\cos(2\theta_M)$. The effective damping coefficient clearly decreases with increasing precession frequency and approaches a constant

value. It can be analytically decomposed into an intrinsic damping coefficient (α_0) and an extrinsic damping (α_{ext}). The former is being regarded independent of the external field, while the latter is due to inhomogeneous broadening and depends on f . Here, $\alpha_0 = 0.006 \pm 0.002$ for this semi-insulating $\text{Cr}_2\text{Ge}_2\text{Te}_6$ is lower than that measured for many ferromagnetic materials with perpendicular magnetic anisotropy [135]. This result may be qualitatively understood by considering two facts that are mostly absent in metallic ferromagnets. First, the deviation of the g -factor of 2.04 ± 0.03 from the free-electron value $g = 2$ indicates a tiny orbital contribution to the magnetization. This points to a weak spin-orbit interaction, which induces spin-phonon scattering and thereby strongly suppresses the transverse magnetization relaxation [136]. In addition, since electrons are mostly localized in a semi-insulating system, spin relaxation due to electron-electron scatterings is highly suppressed in this layered $\text{Cr}_2\text{Ge}_2\text{Te}_6$. In contrast, the overall α_{eff} obtained in Fe_3GeTe_2 via electron spin resonance are large with an average value of about 0.58 and it appears no dependence on temperature in the vicinity of $T_c \sim 200$ K [137]. There have three possible sources accounting for the large damping α_{eff} value: first, Fe_3GeTe_2 as an itinerant ferromagnet owns a huge intrinsic Gilbert damping; second, strong magnon scattering process can be an additional magnetic relaxation channel near T_c and causes the enhancement of linewidth and damping; third, magnetization inhomogeneity may contribute to the damping in this material.

The magnetization dynamics in CrI_3 have been studied using an ultrafast optical pump/magneto-optical Kerr probe technique [134]. Figure 8e shows the time evolution of the pump-induced Kerr rotation of bilayer CrI_3 under in-plane magnetic field in the range 0 – 6 T. For all the fields, the MOKE signal shows a sudden change at time zero, followed by an exponential decay on the scale of tens to hundreds of picoseconds. This reflects the incoherent demagnetization process, in which the magnetic order is disturbed instantaneously by the pump pulse and slowly goes back to equilibrium. The frequency of the oscillations can be extracted by fast Fourier transform (FFT, see Fig. 8f) of the time traces after subtraction of the exponentially decaying demagnetization dynamics. As shown in Fig. 8g, a high-energy (ω_h) and a low-energy (ω_l) mode are identified, which are attributed to the two spin-wave eigenmodes (see inset) associated with the antiferromagnetic bilayer. Below about 3.3 T, the two initially degenerate modes split. Although both modes soften with increasing field, ω_l drops nearly to zero frequency. Above 3.3 T, both modes show a linear increase in frequency with a slope equal to the electron gyromagnetic ratio ($\gamma/2\pi = 28$ GHz/T). The latter is a characteristic of ferromagnetic resonance in high fields and 3.3 T is a saturation field that required to fully align the magnetization in-plane. The field-dependence of the spin-wave dynamics can be fully modeled by the coupled LLG equations (see dashed lines in Fig. 8g). The damping rate can be evaluated using $(2\pi/\omega\tau)$, where τ is the spin-wave dephasing time. As shown in Fig. 8h, the damping is higher below and near saturation. In this regime, the mode frequencies are strongly dependent on internal magnetic interactions, which are sensitive to local inhomogeneity. It is worth noting that the sample is a bilayer CrI_3 –monolayer WSe_2 heterostructure. The magnetic resonance involves exciton generation in WSe_2 by the optical pump, followed by ultrafast exciton dissociation and electron transfer at the $\text{CrI}_3/\text{WSe}_2$ interface, and an impulsive perturbation to the magnetic interactions in CrI_3 by the hot carriers. The spin-wave amplitude thus strongly depends on the pump wavelength.

4.2. Exciton-magnon coupling

Atomically thin flakes of CrSBr maintain the bulk magnetic structure down to the ferromagnetic monolayer with a Curie temperature $T_C = 146$ K and to the antiferromagnetic bilayer with a Néel temperature $T_N = 140$ K [138]. CrSBr is also a direct-gap semiconductor down to the monolayer, with an electronic gap of 1.5 eV and an excitonic gap of 1.34 eV [139]. The coexistence of both magnetic and semiconducting properties implies that a spin wave may coherently modulate the electronic structure. As a result, such exciton-magnon coupling allows the launch and detection of spin waves from strong absorption, emission or reflection of light in the energy range corresponding to excitonic transitions. Based on first-order perturbation theory, the shift in the exciton energy (ΔE_{ex}) owing to changes in the interlayer electron-exchange interaction can be evaluated by $\Delta E_{\text{ex}} \propto \cos^2(\theta/2)$ where θ is the angle between the magnetic moments in neighboring layers [140]. In the AFM state ($\theta = \pi$), the interlayer hybridization is spin forbidden and $\Delta E_{\text{ex}} = 0$; in the FM state ($\theta = 0$), the interlayer electron-exchange interaction is the greatest and ΔE_{ex} is -20 meV [140]. The dependence of ΔE_{ex} on θ is the basis for exciton sensing of coherent spin waves [141].

To investigate the dynamical change in ΔE_{ex} , CrSBr is excited by a femtosecond laser pulse with above-gap photon energy ($h\nu_1 = 1.7$ eV) and the change in reflectance at a variable time delay (Δt) is measured by a broadband probe pulse ($h\nu_2 = 1.3 - 1.4$ eV) [141]. As shown by the static reflectance spectrum in Fig. 9a, the peaks in $\Delta R/R$ correspond to excitonic transitions. Upon photoexcitation, the strong oscillatory components in Fig. 9b come from the coherent magnons and the coupling between excitons and coherent magnons is revealed by clear π -phase flips of the oscillatory signal at the excitonic transitions [142, 143]. The frequencies of the coherent magnons can be determined by an FFT of the oscillatory signal, yielding $\nu_{\text{mag}1} = 24.6 \pm 0.7$ GHz and $\nu_{\text{mag}2} = 34 \pm 1$ GHz (see inset of Fig. 9c for a typical FFT spectrum at $T = 5$ K). With increasing temperature, the magnetic order decreases and

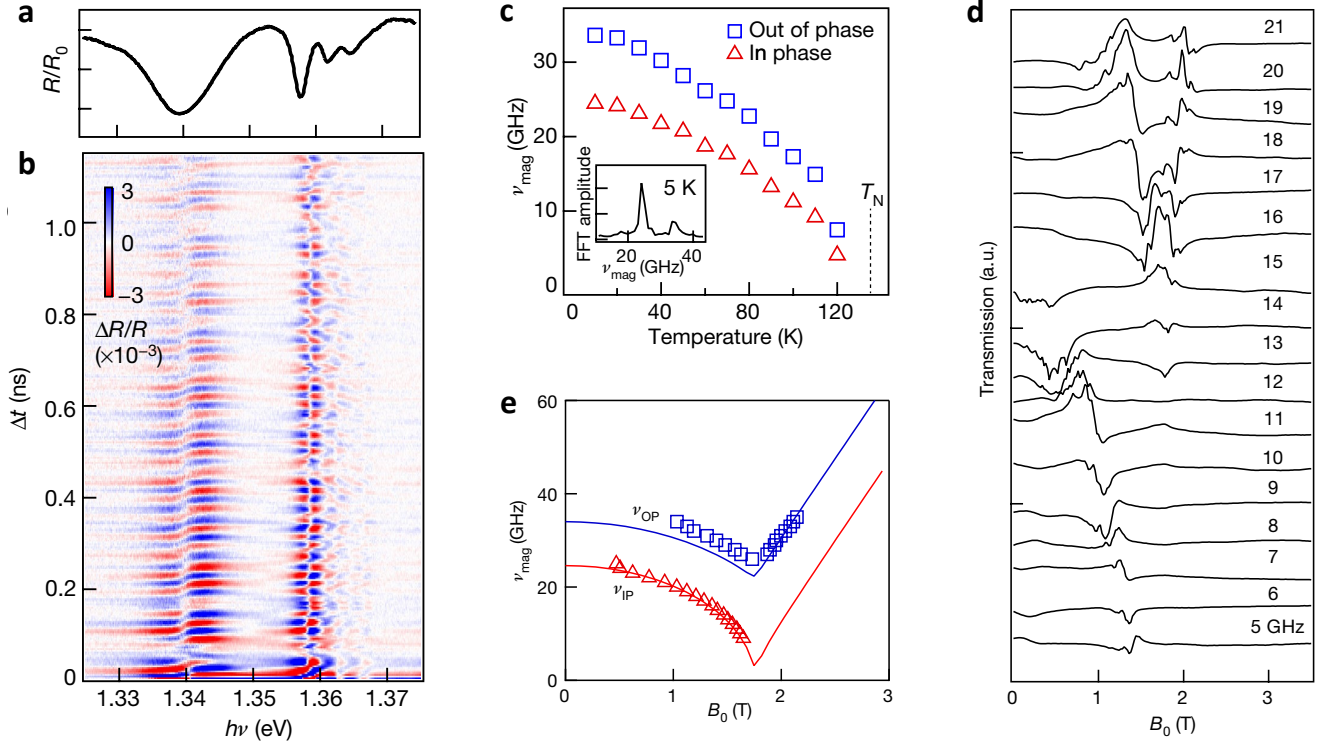


FIG. 9. **a.** Reflectance (R) from CrSBr normalized to that of the SiO_2 substrate (R_0). **b.** Transient reflectance spectra $\Delta R/R$ as a function of pump-probe delay (Δt) and probe photon energy ($h\nu$). An incoherent background has been subtracted from $\Delta R/R$. The pseudo-color scale is $\Delta R/R$, where R is reflectance without pump and ΔR is pump-induced change in reflectance. **c.** The two spin-wave frequencies are shown as a function of sample temperature below T_N . The inset is the probe $h\nu$ -integrated FFT trace showing the two peaks at 24 GHz and 34 GHz at 5 K. **d.** Magnetic resonance spectra at the indicated frequencies (5–21 GHz) from a bulk CrSBr crystal at $T = 5$ K, with the magnetic field applied along the c axis. The spectra are offset for clarity. **e.** Peak resonance frequencies as a function of magnetic field (symbols). The solid curves are dispersion fits from linear spin-wave theory. All panels are adapted from Ref. [141]

this results in lowering of the spin-wave frequencies (Fig. 9c). Around T_N , both $\nu_{\text{mag}1}$ and $\nu_{\text{mag}2}$ approach zero. The temperature dependence of $\nu_{\text{mag}1}$ and $\nu_{\text{mag}2}$ closely follows that of the magnetic-order parameter [138].

The assignments of coherent magnon modes from excitonic sensing are supported by magnetic resonance spectroscopy. Figure 9d shows a series of magnetic resonance spectra at selected microwave frequencies ($\nu = 5\text{--}21$ GHz) for bulk CrSBr at $T = 5$ K. The spectra reveal a single resonance in the low-frequency (≤ 18 GHz) region and two resonances in the high-frequency (> 22 GHz) region. As shown in Fig. 9e, the peak frequencies of the resonances are plotted as a function of the magnetic field applied along the c axis (B_0). For B_0 smaller than a saturation field ($B_{\text{sat}} \approx 1.7$ T), two branches of magnons are observed whose frequencies decrease with increasing B_0 , consistent with the reduction in AFM order as spins are progressively canted away from the easy b axis. The frequencies of these two branches are assigned to the in-phase (ν_{IP}) and out-of-phase (ν_{OP}) spin precessions, similar to those observed in the 2D AFM materials of chromium chloride and chromium iodide [123, 134]. Above B_{sat} , the spins are fully polarized parallel to B_0 and ν_{mag} increases linearly with B_0 , which is expected for a ferromagnetic resonance. The magnetic resonance spectroscopy data can be fitted to a linear spin-wave theory (solid curves in Fig. 9e) [147].

5. Spin-Torque FMR

Spin current injected into a ferromagnetic material produces a spin-transfer torque (STT) [148], which is essential for low-power manipulation of magnetization in spintronic devices, such as magnetic random-access memory, race-track memory, and logic circuit [149–154]. Recently, many studies have been reported on the STT of spin currents generated by the spin Hall effect [155–159] and the Rashba-Edelstein effect [160–162], where momentum locking due to spin-orbit coupling (SOC) plays a significant role in the spin-current generation [163]. In particular, the emergence

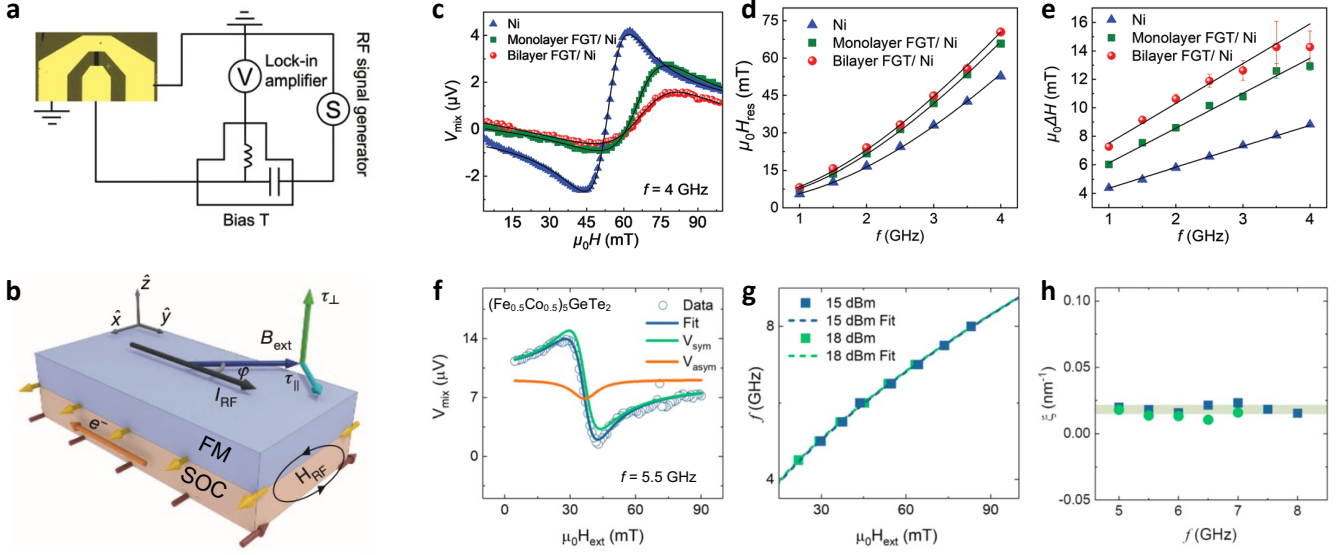


FIG. 10. **a.** Optical image of the sample geometry including contact pads, with the circuit used for ST-FMR measurements. **b.** Schematic diagram of the SOC/FM bilayer structure and coordinate system. The yellow and red arrows denote spin moment directions. I_{RF} and H_{RF} represent the applied radio frequency current and the corresponding Oersted field. An external magnetic field B_{ext} in the film plane at a ϕ angle with respect to the current direction **c.** Typical ST-FMR spectra of Ni (blue), monolayer-FGT/Ni (green) and bilayer-FGT/Ni (red) recorded at 4 GHz at room temperature. Frequency dependence of **d.** the resonance field and **e.** the linewidth of these devices. **f.** The ST-FMR signal of an FCGT/ $\text{Co}_{0.9}\text{Fe}_{0.1}$ sample at 5.5 GHz, 18 dBm. The solid lines are fits that show the symmetric (orange) and antisymmetric (yellow) Lorentzian contribution. **g.** ST-FMR frequency as a function of resonance field; the blue (15 dBm) and green (18 dBm) line is a fit to the Kittel formula. **h.** Charge to spin conversion coefficient (ξ) as a function of frequency at 15 and 18 dBm. Panels **a**, **c-e** are adapted from Ref. [144]. Panels **b** are adapted from Ref. [145]. Panels **f-g** are adapted from Ref. [146].

of vdW magnets has stimulated growing interest in the exotic spin transport phenomena in spintronic devices. One of the major tasks of these studies is to evaluate the spin Hall angle, which represents the conversion ratio of the generated spin current to the injected charge current [164–166].

Spin-torque ferromagnetic resonance (ST-FMR) uses current-induced spin-torques to induce spin precession [167]. It usually requires the patterning of a spin-orbit-coupling/ferromagnet (SOC/FM) bilayer sample (see Fig. 10b) to strips of micrometer scale. Figure 10a shows the sample configuration with coplanar waveguide patterns for microwave input and signal detection [145]. As shown in Fig. 10b, the microwave induced an oscillating transverse spin current in the SOC layer. This spin current is injected into the magnetic layer exciting spin precession and generating an RF anisotropic magnetoresistance. This magnetoresistance, rectified with the microwave current, generated a DC voltage. The ST-FMR spectrum can be obtained by sweeping external in-plane magnetic fields through the resonance condition. The ST-FMR signal (V_{mix}) can be fitted to the field-derivative lineshape in Eq. (2). The two vector components of the current-induced torque, along the in-plane $\tau_{\parallel} \propto m \times (m \times \sigma)$ and out-of-plane $\tau_{\perp} \propto m \times \sigma$ directions (see Fig. 10b), are respectively obtained from the amplitudes of the symmetric (A_{sym}) and anti-symmetric (A_{asy}) components of the resonance lineshape. As a result, the spin Hall angle can be evaluated from the ratio $A_{\text{sym}}/A_{\text{asy}}$:

$$\theta_{\text{SH}} = \frac{A_{\text{sym}}}{A_{\text{asy}}} \left(\frac{e\mu_0 M_s t_{\text{FM}} t_{\text{SOC}}}{\hbar} \right) \left[1 + \frac{4\pi M_{\text{eff}}}{H_{\text{ext}}} \right]^{1/2} \quad (15)$$

where e is the electron charge, μ_0 is the permeability of vacuum, M_s is the saturation magnetization, \hbar is the reduced Planck's constant, and t_{FM} and t_{SOC} is the thickness of the magnet and SOC layer, respectively.

ST-FMR has been employed to study the proximity effect in a device that consists of a Fe_3GeTe_2 (FGT) flake and Ni thin films [144]. Figure 10c shows the typical ST-FMR spectra recorded from three series of devices: Ni, monolayer-FGT/Ni and bilayer-FGT/Ni. The symmetric components of these spectra are close to zero, indicating the negligible spin-orbit torques induced by Au contact pads. The spectra demonstrate the modulation of Ni magnetism by FGT, evident by the increasing resonance field (H_{res}) and linewidth (ΔH) when Ni is integrated with monolayer and bilayer FGT. H_{res} as a function of frequency are shown in Fig. 10d. Based on the fitting to a Kittel equation, one can identify a decreasing M_{eff} going from the Ni device to the monolayer-FGT/Ni and bilayer-FGT/Ni devices. The

decreased M_{eff} value in FGT/Ni may be attributed to the increase of the perpendicular magnetic anisotropy (PMA) in Ni. Apart from the interfacial d - d hybridization, the increased PMA of Ni may be associated with the interlayer magnetic exchange coupling between the Fe and Ni atoms.

Moreover, the FGT interface also leads to enhanced magnetic damping in Ni, as indicated by the frequency dependence of and ΔH shown in Fig. 10e. The frequency-dependent linewidths can be well fitted using

$$\Delta H = \Delta H_0 + \frac{4\pi\alpha}{\gamma} f \quad (16)$$

where ΔH_0 is the linewidth at zero frequency determined by inhomogeneous broadening, and α is the Gilbert damping of Ni. The increased inhomogeneous broadening may result from interfacial magnetic coupling, which gives rise to the inhomogeneous magnetization texture [144, 168]. The enhanced Gilbert damping suggests additional loss of the spin angular momentum, which may be attributed to the spin pumping effect and the exchange coupling between the Fe and Ni atoms.

Another significant work is ST-FMR measurements of $(\text{Fe}_{0.5}\text{Co}_{0.5})_5\text{GeTe}_2$ (FCGT, 21 nm, ~ 11 unit cells) on $\text{Co}_{0.9}\text{Fe}_{0.1}$ (12 nm) [146]. AA'-stacked FCGT is a wurtzite-structure polar magnetic metal ($T_c \sim 350$ K) with broken spatial inversion and time reversal symmetries. It exhibits a Néel-type skyrmion lattice as well as a Rashba-Edelstein effect at room temperature. A typical ST-FMR signal for an AA'-FCGT/ $\text{Co}_{0.9}\text{Fe}_{0.1}$ is shown in Fig. 10f. The spectrum can be fitted well to a sum of symmetric and asymmetric components, and ST-FMR frequency as a function of resonant field (see Fig. 10g) is in good agreement with the Kittel formula. The charge-to-spin conversion coefficient (ξ), represented by θ_{SH} in Eq. (15), as a function of frequency is essentially constant, as shown in Fig. 10h. The average ξ of the AA'-FCGT/ $\text{Co}_{0.9}\text{Fe}_{0.1}$ system is $\sim 0.017 \pm 0.003 \text{ nm}^{-1}$. The ST-FMR signal of the AA'-FCGT/ $\text{Co}_{0.9}\text{Fe}_{0.1}$ sample may originate from the Rashba-Edelstein effect of the Te/ $\text{Co}_{0.9}\text{Fe}_{0.1}$ interface or the spin Hall effect from the AA'-FCGT system. Even though the second-harmonic Hall signal was observed in the single-layer AA'-FCGT, more approaches are still needed to distinguish the contributions of the ST-FMR signal in detail in future work.

TABLE II. Magnetic properties of emerging vdW magnets and prototypical bulk magnets.

Material	g_{\perp}	g_{\parallel}	H_k (kG)	α	T_c (K)	Synthesis method	Reference
CrCl_3	1.970 (100 K)	1.990 (100 K)	~ 0	-	17(bulk)	CVT	[89]
CrI_3	2.07 (1.5 K)	-	28.6 (1.5 K)	-	70 (bulk) 45 (ML)	CVT, MBE	[97]
CrBr_3	-	-	5.6 (10 K)	0.009 (10 K)	47	CVT, flux	[119]
Fe_5GeTe_2	1.99 (300 K)	2.21 (300 K)	1.8 (300 K)	0.035 (300 K)	300	CVT, CVD, MBE	[108]
CrSiTe_3	2.70 (34 K)	1.75 (34 K)	20 (2 K)	-	34.15	flux	[34]
$\text{Cr}_2\text{Ge}_2\text{Te}_6$	2.10 (2 K)	2.18 (2 K)	5.82 (2 K)	0.01-0.08 (10 K)	64.7	CVT, flux	[133]
Fe_3GeTe_2	-	-	12 (185 K)	0.58 (185 K)	150-220	CVT, MBE	[137]
$\text{Y}_3\text{Fe}_5\text{O}_{12}$ (YIG)	2 (300 K)	2 (300 K)	0.09-0.4 (300 K)	8.58×10^{-5} (300 K)	567	Sputtering, PLD	[169]
NiFe	2 (300 K)	2 (300 K)	0	0.005-0.008 (300 K)	553 (bcc) 872 (fcc)	Sputtering, MBE	[170]

CVT: Chemical vapor transport; MBE: molecular beam epitaxy; CVD: Chemical vapor deposition; PLD: Pulsed laser deposition.

TABLE III. Comparison between different FMR techniques and methodologies.

Technique	Spin excitation methods	Detection methods	Sample requirements	Unique capabilities
Broadband FMR	Microwave injected through co-planar waveguide	Microwave absorption	Bulk crystals, thin films	It has high flexibility and is compatible with cavity resonator to enhance the sensitivity
Optical FMR	Optical pump using ultra-fast laser pulses	Magneto-optical Faraday/Kerr effect, transient reflectivity, x-ray magnetic circular dichroism	Bulk crystals, thin films, exfoliated thin flakes	It has spatial resolution for mapping domain structures and time-resolution for measuring spin relaxation time.
Spin-torque FMR	Microwave current injected through on-chip coplanar waveguide pattern	DC voltage generated from the rectification between AC current and resistance oscillation	Heavy metal/ferromagnet bilayer structures, exfoliated thin flakes,	It provides direct access to the spin-torque induced spin-charge conversion

6. Conclusion and Perspective

Advances in the 2D vdW magnet exploration have spurred new interests in spintronics. As we have discussed above, probing spin dynamics provides access to key parameters such as the exchange interaction, magnetic anisotropy, g -factor, spin-wave eigenmodes, and spin-orbit torque in 2D vdW magnets and heterostructures, which is crucial for designing ultra-fast spintronic devices. The magnetic properties including g -factors extracted from FMR along $H \parallel c$ (g_{\perp}) and $H \parallel ab$ (g_{\parallel}), effective magnetization (H_k), damping rate (α), transition temperature (T_c), and synthesis method for emerging vdW magnets and prototypical bulk magnets (yttrium iron garnet, or YIG) and magnetic thin films (NiFe) are summarized in Table II.

Moreover, vdW magnets can be used to build tunable magnon-magnon coupling, which have vast applications in quantum transduction and entanglement applications [171]. Using vdW assembly such as moiré lattice, one can combine different magnetic materials to induce magnon-magnon coupling without out-of-plane field by breaking sublattice exchange symmetry. In addition, recent simulation works suggest that synthetic vdW magnets exhibit both dipolar coupling and Ruderman–Kittel–Kasuya–Yosida (RKKY) exchange coupling among multiple vdW sublattices, which open up new opportunities for very strong magnon hybridization [172, 173]. These intriguing physics and promising applications will attract great interest in ferromagnetic resonance studies of the microscopic quantities associated with spin dynamics and magnon hybridization. Moreover, electric field can be used to modulate the resonance frequency, damping and coupling strength in vdW magnet-based magnonic devices. A recent theoretical work predicts electric field controlled magnonic dynamics at exceptional points in a parity–time symmetric waveguide [174]. ST-FMR thus provides a powerful tool to investigate and realize such spin-orbit interaction driven interfacial phenomena.

Looking forward, we envision many emergent spin dynamics probes will be applied to study 2D vdW magnets. Here, the comparison between broadband FMR, optical FMR, and spin-torque FMR techniques is summarized in Table III. In addition, we highlight several recent technical advances in probing phase-resolved magnetic dynamics, magnon-phonon hybridization, local probe of spin transport, and element-specific magnetization dynamics. In addition to unravel fundamental properties, these techniques involving fiber-based magneto-optical detection, superconducting resonator, and nitrogen-vacancy magnetometry also represent promising applications in hybrid quantum magnonic devices and quantum sensing.

6.1. Magneto-optical detection of phase-resolved ferromagnetic resonance

The development in quantum magnonics [177–179] highlight the needs for detecting spatial- and phase-resolved magnetization dynamics adaptable to micro- and nano-scale magnonic devices with synergistic photonic and spin-electronic components on-chip. This technique operating at the telecommunication wavelength at 1550-nm has been recently developed [175, 180]. It takes advantage of the conventional microwave excitation of FMR and synchronizes such excitation with a GHz-modulated optical probe. A schematic illustration of the experimental setup is shown in

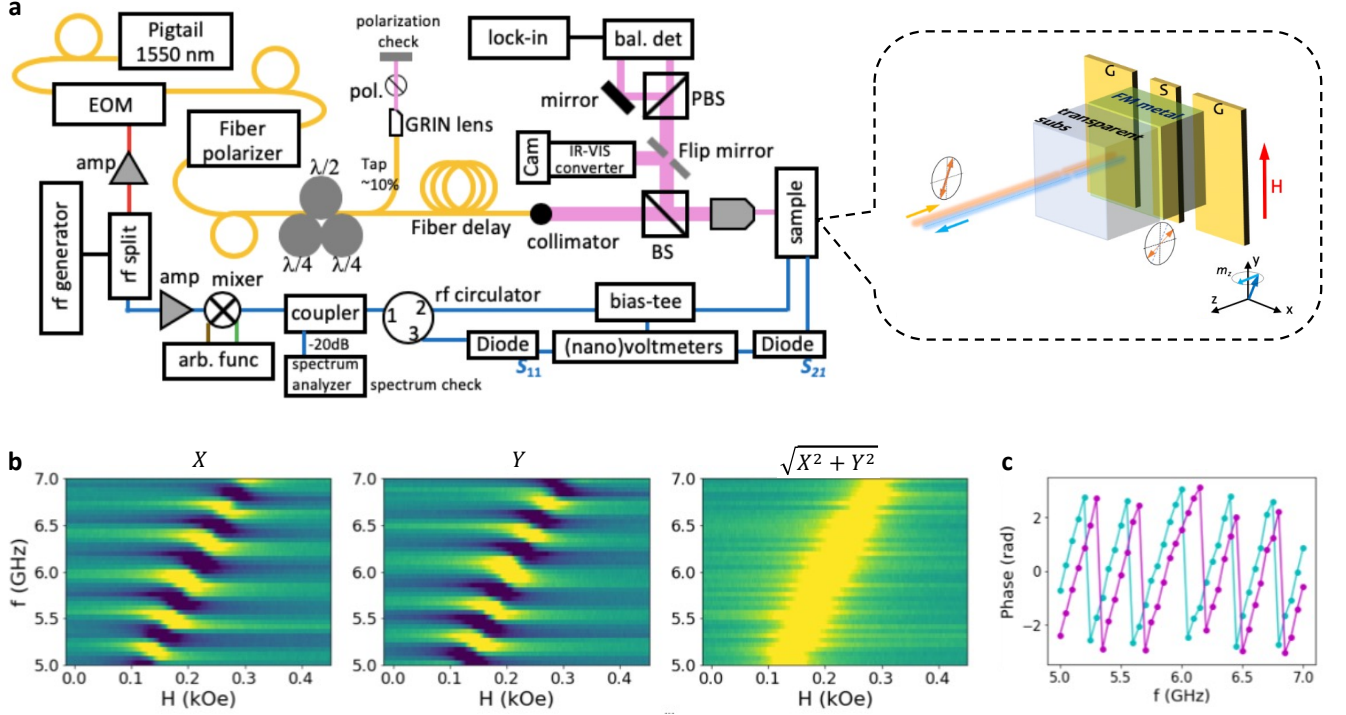


FIG. 11. **a.** Schematic of the optical detection of phase-resolved magnetization dynamics setup. After the rf splitter, the optical path (upper part) contains amplifier, 1550-nm infrared laser module, electro-optic modulator (EOM), fiber polarizer, fiber polarization controller, beam splitter (BS) and focusing lens; the electrical path (lower part) contains amplifier, mixer, coupler, spectrum analyzer, diodes, circulator, bias-tee, and nanovoltmeter. (PBS = polarizing beam splitter, Cam = camera, bal.det = balanced detector, arb. func = arbitrary waveform generator.) The dashed box shows the detecting mechanism for the dynamic Kerr effect. The applied DC magnetic field is parallel to the ground-signal-ground (G-S-G) lines of the coplanar waveguide. **b.** The intensity map of the FMR scan (5.0–7.0 GHz) for the Fe/Pt bilayer of the in-phase (X) and quadrature (Y) components, and total amplitude ($\sqrt{X^2 + Y^2}$) as a function of the magnetic field and frequency. **c.** The phase evolution as a function of frequency. All panels are adapted from Ref. [175].

Fig. 11a. The setup allows facile modulation at the GHz frequencies with both amplitude and phase controls and also phase-locking to a microwave source for FMR excitation. Figure 11b shows the intensity map of the FMR scan for the Fe/Pt bilayer. The optical signals with the phase information are obtained by the lock-in amplifier’s in-phase (X) and quadrature (Y) components. The total amplitude calculated by $\sqrt{X^2 + Y^2}$ resembles the conventional microwave diode measurements and the extracted phase evolution is shown in Fig. 11c.

Such a continuous-wave (CW) modulation capability makes this particular wavelength-band advantageous for studying magnetization dynamics in complex magnetic systems [181–185], such as quantum magnonic hybrids, patterned nanomagnets, spin ice, and 2D magnets. Compared to visible light wavelengths for magneto-optics, the method allows for the coherent tracking of gigahertz spin dynamics in a CW fashion, very much resembling a “lock-in” type of measurement that is commonly performed in many low-noise electric and spin transport measurements. In addition, the fiber-based optics allow for a compact integration with simultaneous electrical, thermal, and magnetic measurements with less susceptibility to typical mechanical vibrations, and therefore, having the advantage of being made into compact, tabletop or even portable systems with yet robust measurement performances for studying 2D magnets and related 2D heterostructures.

6.2. Magnon-photon coupling probed in a superconducting resonator

The interaction between microwave photons and magnons is determined by the mode volume overlap between the two. This essentially means that when we aim to probe spin dynamics of 2D vdW monolayers (which are typically μm sized flakes) using microwave photons, the photon mode must have a correspondingly small mode size to maximize the coupling strength and hence its sensitivity. One of the promising approaches to this is to use on-chip superconducting

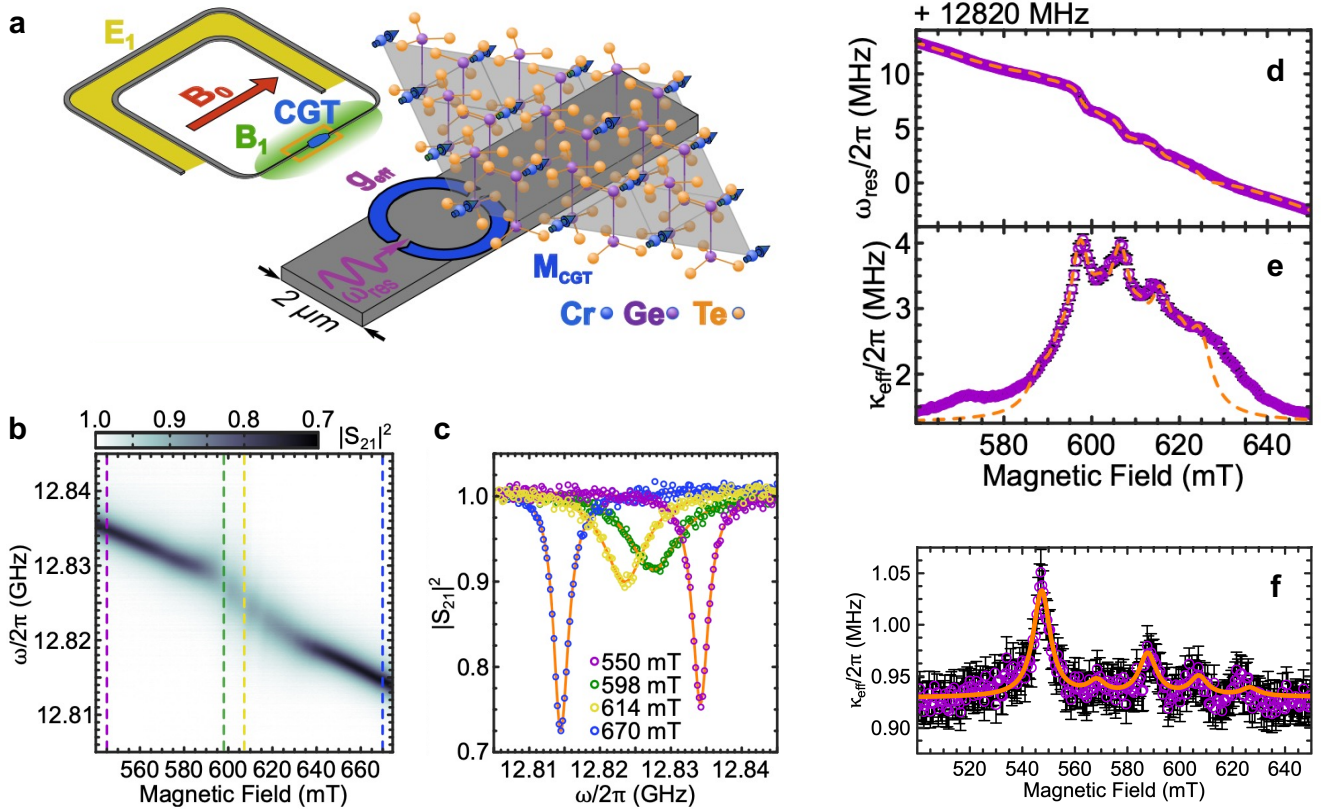


FIG. 12. **a**. Schematic of a superconducting resonator indicating the areas of high E_1 -field (yellow) and B_1 -field (green) intensities, as well as the orientation of the externally applied field B_0 . A zoom in of the section loaded with a $\text{Cr}_2\text{Ge}_2\text{Te}_6$ flake is shown. **b**. $|S_{21}|^2$ as a function static magnetic field B_0 and frequency, with the microwave transmission encoded in the color. **c**. $|S_{21}|^2$ as a function of frequency at fixed magnetic fields, indicated in **b** by dashed vertical lines. **d** and **e**. Resonance frequency ω_{res} and effective loss rate κ_{eff} as a function of magnetic field. The dashed orange lines are results from the semi-optimized fit. **f**. Effective loss rate κ_{eff} as a function of magnetic field of a resonator loaded with the thinnest CGT sample ($\sim 11\text{nm}$). All panels are adapted from Ref. [176].

(SC) resonators [176, 186, 187]. Strong coupling between photons in SC resonators and magnons in anti-ferromagnetic CrCl_3 bulk systems has been demonstrated [186, 187].

Zollitsch *et al.* recently reported that it is possible to probe spin dynamics of $\text{Cr}_2\text{Ge}_2\text{Te}_6$ as thin as 11 nm using SC resonators [176]. $\text{Cr}_2\text{Ge}_2\text{Te}_6$ flakes were exfoliated and transferred onto magnetically-active parts of high-quality-factor SC lumped element resonators with their small mode volume ($\approx 6000\ \mu\text{m}^3$), as schematically shown in Fig. 12a. The SC resonators are coupled to a microwave transmission line, through which the SC resonance modes are monitored. Figure 12b displays a 2D color map of the microwave transmission coefficient (S_{21}) as a function of both external magnetic field and frequency. A clear SC photon mode is visible and the spectral distortion of the photon mode is found in a magnetic field range (590-620 mT) where the magnon Kittel mode is expected to have the same resonance frequency as the photon mode. As shown in Fig. 12c, this causes the observable linewidth broadening for the particular field range, which can be analysed by using a phenomenological model of coupled harmonic oscillators [176]. The photon mode frequency (ω_{res}) as well as the relaxation rate of the hybrid magnon-photon modes (κ_{eff}) were extracted by the spectral data as shown in Fig. 12d and 12e. κ_{eff} is strongly enhanced due to the large relaxation rate of CGT magnons and using the plot shown in Fig. 12e, the spin dynamics of the CGT magnon modes can be analysed (see details in [176]). They also demonstrated the photon-magnon coupling using a 11 nm CGT flake (Fig. 12f) where the CGT magnon modes are still detected through this measurement scheme. It turns out that CGT magnon modes have a large dissipation rate, posing a fundamental bottleneck for achieving the strong coupling at this limit. However, multiple avenues for improving the coupling strength are available to overcome this challenge. Such as by introducing nm-scale constrictions with resonator mode volume reduction [189, 190], and mode overlap enlargement using large-scale 2D vdW material transfer techniques [191]. With the successful creation of coherent photon-magnon hybrids (magnon-polaritons), they can be used for efficient energy-transfer between polaritonic states with different

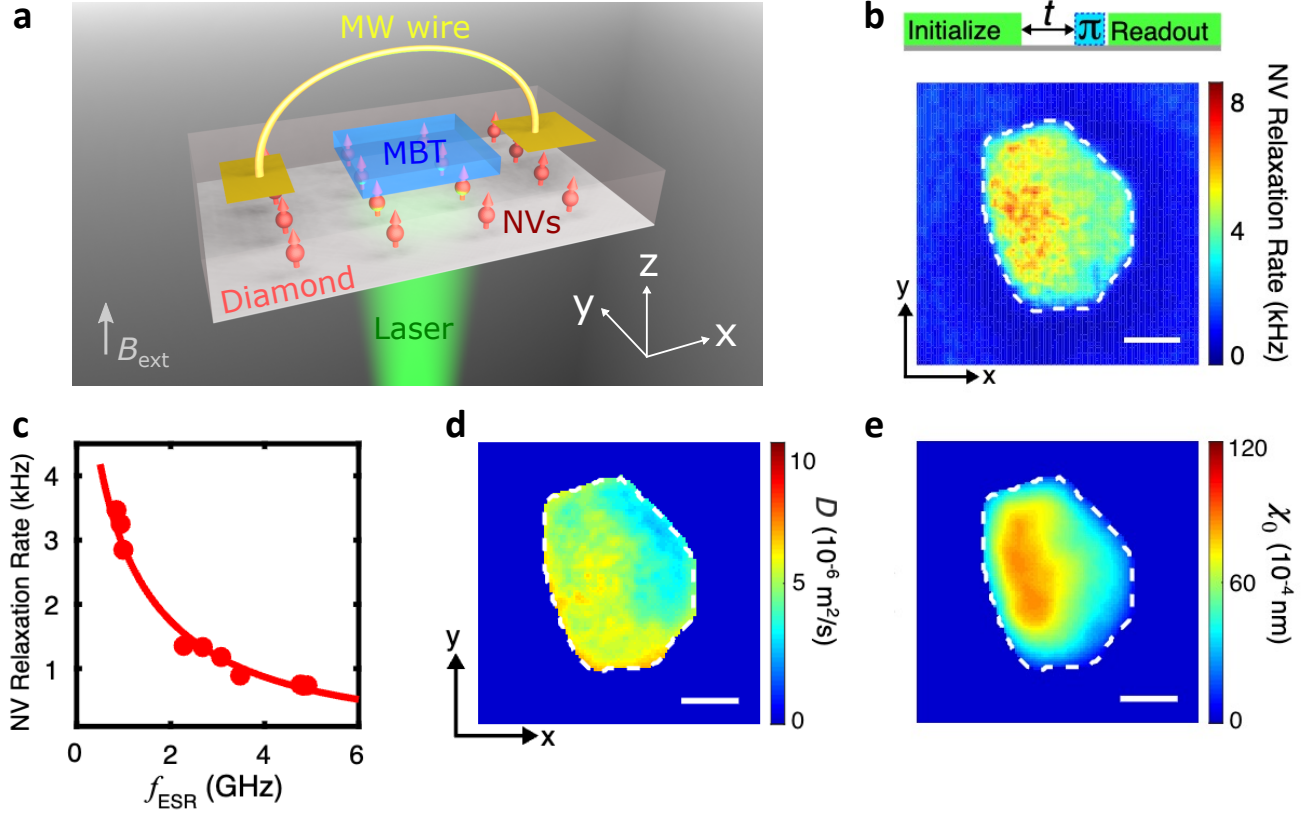


FIG. 13. **a.** Schematic of an NV wide-field magnetometry measurement platform. **b.** NV spin relaxation map measured for an exfoliated MnBi₄Te₇ (MBT) flake at ESR frequency f_{ESR} of 1.0 GHz at 8.5 K. The boundary of the MBT flake is outlined with white dashed lines. **c.** Spatially averaged NV spin relaxation rates measured on the MnBi₄Te₇ flake (red dots) as a function of f_{ESR} at 8.5 K. The experimental results are in excellent agreement with the theoretical prediction (red curve). **d-e.** 2D images of spin diffusion constant (D) and magnetic susceptibility (χ_0) of the MBT flake at 8.5 K. The scale bar is $4 \mu\text{m}$. All panels are adapted from Ref. [188].

degrees of freedom in vdW systems [192, 193].

6.3. Nitrogen-vacancy electron spin resonance

Advanced quantum sensing techniques provide another perspective to investigate the rich physics of 2D magnets. Nitrogen-vacancy (NV) centers, optically active spin defects in diamond, are a prominent candidate in this category [194]. Over the past years, NV magnetometry techniques have been demonstrated as a transformative tool in exploring the local static and dynamic spin behaviors in 2D magnets with competitive field sensitivity and spatial resolution. Examples include nanoscale imaging layer-dependent 2D magnetization [195], 2D magnetic domains [196], magnetization reversal processes [197], moiré magnetism [198], room-temperature 2D ferromagnetism [199, 200], and others [188, 201]. Here, we briefly discuss the opportunity to use NV relaxometry method to probe intrinsic spin fluctuations in 2D magnetic materials, which is challenging to access by conventional magnetometry techniques.

Figure 13a shows a schematic of NV-based wide-field imaging platform. An MnBi₄Te₇ nanoflake is transferred onto the diamond surface with shallowly implanted NV ensembles [188]. Figure 13b show an example of the 2D NV relaxation maps. NV relaxometry measurements take advantage of the dipolar interaction between spin density of a magnetic sample and proximate spin sensors [188, 205–207]. At thermal equilibrium, fluctuations of the longitudinal spin density will generate low-frequency fluctuating magnetic fields at the NV electron spin resonance frequencies f_{ESR} , resulting in enhancement of NV relaxation rates. By measuring the NV relaxation rate as a function of f_{ESR} and fitting it into a theoretical model (Fig. 13c), we can extract key material parameters such as local spin diffusion constant (D) and magnetic susceptibility (χ_0) of the MnBi₄Te₇ flake as shown in Fig. 13d and 13e [188].

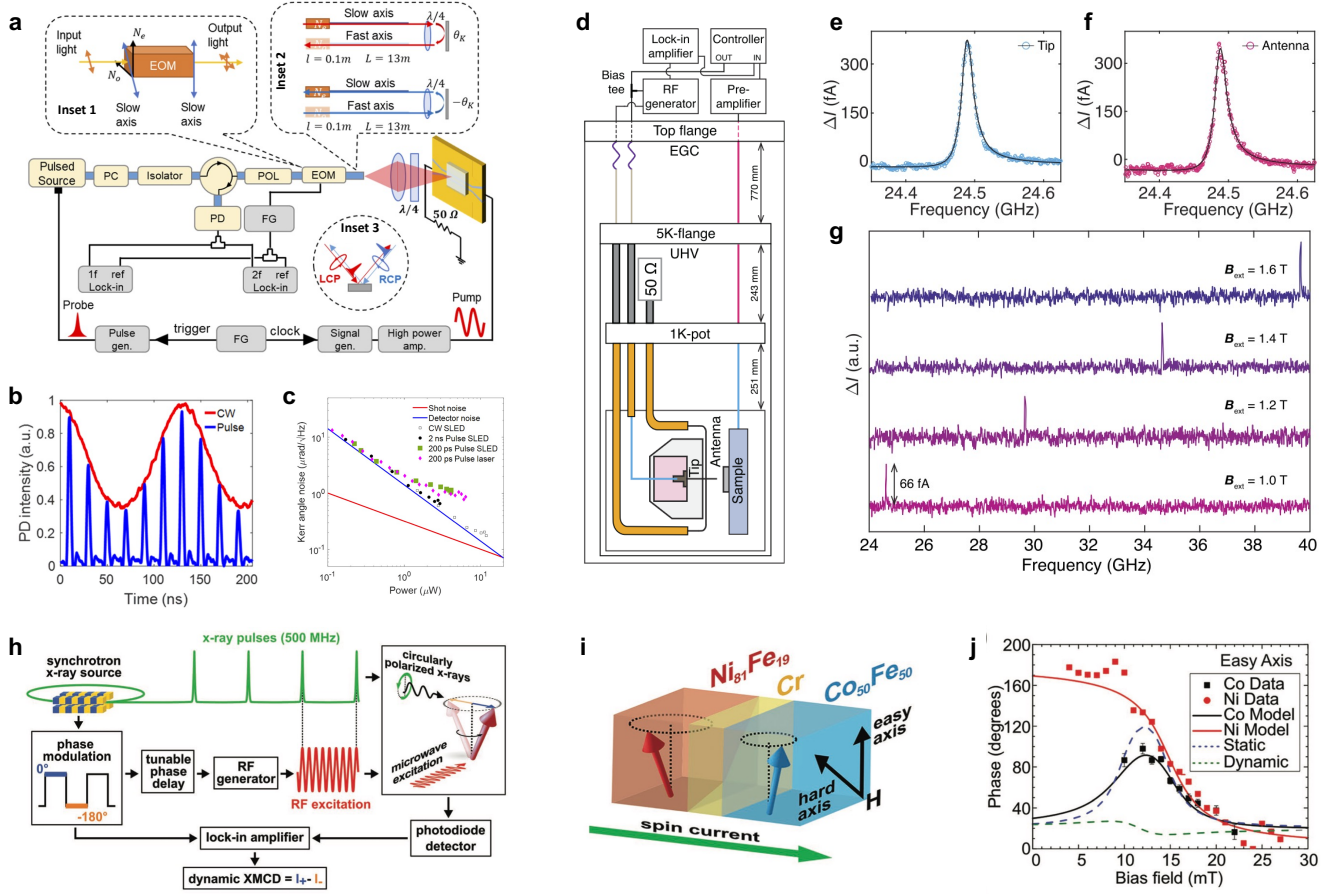


FIG. 14. **a.** Schematic of the time-resolved zero-area Sagnac interferometer (TR-ZASI). PC: polarization controller, POL: polarizer, PD: photoreceiver, and FG: function generator. Inset 1: The polarization axis of the electro-optic modulator (EOM). Inset 2: The two counterpropagating paths in the TR-ZASI. Inset 3: Optical pulses near the sample. LCP (RCP) means left (right) circular polarization. **b.** Experimental intensity of the interferometer for continuous wave (CW) and pulse modes measured by a 125 MHz photoreceiver and 500 MHz digitizer. **c.** Noise characteristics of TR-ZASI for varying light sources. **d.** Wiring scheme for electron spin resonance scanning tunneling microscopy (ESR-STM). Two methods are adopted to apply RF voltages to the tunnel junction: STM tip and RF antenna. **e-f.** Comparison of ESR spectra measured using the tip and the antenna for RF transmission. **g.** ESR spectra of hydrogenated titanium (TiH) atoms at varying magnetic fields measured using the antenna. **h.** Synchrotron-based x-ray detected FMR setup. **i.** Architecture of $\text{Ni}_{81}\text{Fe}_{19}/\text{Cr}/\text{Fe}_{50}\text{Co}_{50}$ spin valve device to generate and detect spin current. **j.** Phase of the $\text{Fe}_{50}\text{Co}_{50}$ spin precession in proximity to the FMR condition of $\text{Ni}_{81}\text{Fe}_{19}$ with field applied along the easy axis of $\text{Fe}_{50}\text{Co}_{50}$. Panels **a-c** are adapted from Ref. [202]. Panels **d-g** are adapted from Ref. [203]. Panels **h-j** are adapted from Ref. [204].

Temperature and magnetic field dependent NV relaxation rate measurements can also be used to reveal the magnetic phase transitions of 2D magnets. It is instructive to note that the spatial resolution of the NV wide-field imaging techniques typically stays in the hundreds of nanometers regime, which is fundamentally set by the optical diffraction limit [197]. For scanning NV microscopy, the spatial sensitivity can ultimately reach the regime of tens of nanometers, offering an attractive platform to reveal the detailed microscopic spin textures and dynamic responses in various 2D quantum materials [208, 209].

6.4. Other technical advances

It is worth noting that 1550 nm CW laser has also been used in the all-fiber design of Sagnac interferometer for magneto-optical measurements of ferromagnetic resonance [210]. Sagnac interferometers have proven as a powerful technique that can measure the magneto-optical Kerr effect with $100 \text{ nrad}/\sqrt{\text{Hz}}$ sensitivity using only a 10 μW optical power without the magnetic field modulation [211–217]. Recently, this technique is employed in the magneto-optical

detection of photoinduced magnetism via chirality-induced spin selectivity in 2D chiral hybrid organic-inorganic perovskites [218]. Moreover, by replacing the CW 1550 nm laser to a pulsed one, Heo *et al* developes a time-resolved zero-area Sagnac interferometer (TR-ZASI) for magneto-optical measurements (see Fig. 14a) [202]. As shown in Fig. 14b, in the pulse mode, similar to the case of continuous wave (CW), each pulse will interfere after propagating the clockwise and counterclockwise loops. Also, it has been demonstrated that the pulse mode and the CW mode give the same calibrated Kerr angle. This technique is then used to measure time-resolved Kerr signal at the FMR of a Permalloy film, and the results are fully consistent with other techniques, such as vector network analyzer. Temporal resolution of hundreds of picoseconds is achieved, maintaining the advantages of the Sagnac interferometer. The analysis of the noise (see Fig. 14c) shows that the TR-ZASI can achieve $1 \mu\text{rad}/\sqrt{\text{Hz}}$ sensitivity at a $3 \mu\text{W}$ optical power in the pulse mode. This technique is expected to contribute to magneto-optical measurements of various fast dynamics in ps and ns ranges.

In recent years, the combination of electron spin resonance and scanning tunneling microscopy (ESR-STM) has been demonstrated as a technique to detect magnetic properties of single atoms on surfaces and to achieve sub-microelectronvolts energy resolution [219]. In an ESR-STM experiment performed in Fe atoms absorbed on MgO thin films, it has been shown that single-atom electron spin resonance properties can be tuned by combing a vector magnet and the field from the spin-polarized STM tip [220]. Moreover, by the mixing of a continuous RF voltage to the STM junction, an rf spin-polarized tunneling current is generated from the magnetic tip, which drives a coherent magnetic precession in a ferromagnetic thin film. Hwang *et al* report a homebuilt ESR-STM incorporated with a Joule-Thomson refrigerator and a two-axis vector magnet [203]. In addition to the early design of wiring to the STM tip, they apply RF voltages using an antenna (see Fig. 14d). Direct comparisons of the ESR spectra measured using these two methods (see Fig. 14e and 14f) shows consistent intensity, lineshape, and resonance frequency, indicating that their mechanisms of ESR driving and detection are the same. As shown in Fig. 14g, the antenna method is employed to measure ESR spectra of hydrogenated titanium (TiH) atoms on MgO/Ag(100) at different magnetic fields. This technique permits the study of nanoscale magnetic systems and magnetic skyrmions [221], bearing great potential for quantum sensing and coherent manipulation of quantum information.

Finally, x-ray pulses from synchrotron radiation enable element, site, and valence state resolution of magnetization and spin dynamics [222, 223]. Therefore, the technique of x-ray detected FMR (XFMR) combines FMR and x-ray magnetic circular dichroism (XMCD), in which the sample is pumped by an RF magnetic field to generate a precession of the magnetization, which is then probed using the XMCD effect with magnetic and chemical contrast. XFMR experiments can be carried out in time-averaged and time-resolved manners. In particular, time-resolved measurements are performed in a transverse geometry, where the magnetization is oriented perpendicular to the incident x-ray pulses [224]. In this geometry, the magnetic moments are continuously excited by the RF field while the response from the phase-dependent magnetization components along the x-ray beam is probed stroboscopically. Time-resolved XFMR can thus be used to measure both amplitude and phase of the spin precession. As shown in Fig. 14h, microwaves are generated at a frequency of the higher harmonic of the storage ring frequency (500 MHz) to ensure a fixed phase relationship between the RF pump field and the probing x-ray pulse. By incrementally delaying the phase of the RF field with respect to the timing of the x-ray pulses, the complete spin precession cycle can be mapped. The phase and chemical resolution of XFMR allow to determine the contribution of interlayer coupling and dynamic coupling of each layer in multilayer samples. As shown in Fig. 14i and 14j, it has unique capabilities to probe spin-transfer torque and spin currents in spin valve devices [204, 225]. These advantages can be applied to study magnetic vdW heterostructures and vdW magnetic tunneling junctions.

7. Acknowledgements

W.J. acknowledges support by NSF EPM Grant No. DMR-2129879 and Auburn University Intramural Grants Program. C.T. acknowledges financial support from the Alabama Graduate Research Scholars Program (GRSP) funded through the Alabama Commission for Higher Education and administered by the Alabama EPSCoR. Y.X., J.I., and W.Z. acknowledge partial support from U.S. National Science Foundation under Grants No. ECCS-1941426 for the preparation of this manuscript. N.J.M. and C.R.D. were supported by the Air Force Office of Scientific Research under Award FA9550-20-1-0319. EJGS acknowledges computational resources through CIRRUS Tier-2 HPC Service (ec131 Cirrus Project) at EPCC (<http://www.cirrus.ac.uk>) funded by the University of Edinburgh and EPSRC (EP/P020267/1); ARCHER UK National Supercomputing Service (<http://www.archer.ac.uk>) via Project d429, and the UKCP consortium (Project e89) funded by EPSRC grant ref EP/P022561/1. EJGS acknowledge the Spanish Ministry of Science's grant program "Europa-Excelencia" under grant number EUR2020-112238, the EPSRC

Open Fellowship (EP/T021578/1), and the University of Edinburgh for funding support.

-
- [1] L. Onsager, “Crystal statistics. I. A two-dimensional model with an order-disorder transition,” *Physical Review* **65**, 117 (1944).
 - [2] R. Plumier, “Neutron diffraction study of magnetic stacking faults in antiferromagnetic K_2NiF_4 ,” *Journal of Applied Physics* **35**, 950–951 (1964).
 - [3] M. Lines, “Examples of two dimensional ordered magnetic systems,” *Physics Letters A* **24**, 591–592 (1967).
 - [4] M. Lines, “Magnetism in two dimensions,” *Journal of Applied Physics* **40**, 1352–1358 (1969).
 - [5] U. Gradmann and J. Müller, “Very thin (2–200 Å) ferromagnetic NiFe films,” *Journal of Applied Physics* **39**, 1379–1381 (1968).
 - [6] U. Gradmann, “Ferromagnetism near surfaces and in thin films,” *Applied Physics* **3**, 161–178 (1974).
 - [7] U. Gradmann, R. Bergholz, and E. Bergter, “Magnetic properties of very thin films,” *Thin Solid Films* **126**, 107–116 (1985).
 - [8] M. Julliere, “Tunneling between ferromagnetic films,” *Physics Letters A* **54**, 225–226 (1975).
 - [9] M. N. Baibich, J. M. Broto, A. Fert, F. N. Van Dau, F. Petroff, P. Etienne, G. Creuzet, A. Friederich, and J. Chazelas, “Giant magnetoresistance of (001)Fe/(001)Cr magnetic superlattices,” *Physical Review Letters* **61**, 2472 (1988).
 - [10] G. Binasch, P. Grünberg, F. Saurenbach, and W. Zinn, “Enhanced magnetoresistance in layered magnetic structures with antiferromagnetic interlayer exchange,” *Physical Review B* **39**, 4828 (1989).
 - [11] B. Dieny, V. S. Speriosu, S. S. Parkin, B. A. Gurney, D. R. Wilhoit, and D. Mauri, “Giant magnetoresistive in soft ferromagnetic multilayers,” *Physical Review B* **43**, 1297 (1991).
 - [12] B. Diény, “Giant magnetoresistance in spin-valve multilayers,” *Journal of Magnetism and Magnetic Materials* **136**, 335–359 (1994).
 - [13] J. S. Moodera, J. Nassar, and G. Mathon, “Spin-tunneling in ferromagnetic junctions,” *Annual Review of Materials Science* **29**, 381–432 (1999).
 - [14] J.-G. J. Zhu and C. Park, “Magnetic tunnel junctions,” *Materials Today* **9**, 36–45 (2006).
 - [15] C. Gong, L. Li, Z. Li, H. Ji, A. Stern, Y. Xia, T. Cao, W. Bao, C. Wang, Y. Wang, *et al.*, “Discovery of intrinsic ferromagnetism in two-dimensional van der Waals crystals,” *Nature* **546**, 265–269 (2017).
 - [16] B. Huang, G. Clark, E. Navarro-Moratalla, D. R. Klein, R. Cheng, K. L. Seyler, D. Zhong, E. Schmidgall, M. A. McGuire, D. H. Cobden, *et al.*, “Layer-dependent ferromagnetism in a van der Waals crystal down to the monolayer limit,” *Nature* **546**, 270–273 (2017).
 - [17] S. Jenkins, L. Rózsa, U. Atxitia, R. F. Evans, K. S. Novoselov, and E. J. Santos, “Breaking through the Mermin-Wagner limit in 2D van der Waals magnets,” *Nature Communications* **13**, 1–8 (2022).
 - [18] S. Tian, J.-F. Zhang, C. Li, T. Ying, S. Li, X. Zhang, K. Liu, and H. Lei, “Ferromagnetic van der Waals crystal VI_3 ,” *Journal of the American Chemical Society* **141**, 5326–5333 (2019).
 - [19] X. Cai, T. Song, N. P. Wilson, G. Clark, M. He, X. Zhang, T. Taniguchi, K. Watanabe, W. Yao, D. Xiao, *et al.*, “Atomically thin CrCl_3 : an in-plane layered antiferromagnetic insulator,” *Nano Letters* **19**, 3993–3998 (2019).
 - [20] Z. Zhang, J. Shang, C. Jiang, A. Rasmita, W. Gao, and T. Yu, “Direct photoluminescence probing of ferromagnetism in monolayer two-dimensional CrBr_3 ,” *Nano Letters* **19**, 3138–3142 (2019).
 - [21] X. Sun, W. Li, X. Wang, Q. Sui, T. Zhang, Z. Wang, L. Liu, D. Li, S. Feng, S. Zhong, *et al.*, “Room temperature ferromagnetism in ultra-thin van der Waals crystals of 1T- CrTe_2 ,” *Nano Research* **13**, 3358–3363 (2020).
 - [22] L. Meng, Z. Zhou, M. Xu, S. Yang, K. Si, L. Liu, X. Wang, H. Jiang, B. Li, P. Qin, *et al.*, “Anomalous thickness dependence of Curie temperature in air-stable two-dimensional ferromagnetic 1T- CrTe_2 grown by chemical vapor deposition,” *Nature Communications* **12**, 1–8 (2021).
 - [23] X. Zhang, Q. Lu, W. Liu, W. Niu, J. Sun, J. Cook, M. Vaninger, P. F. Miceli, D. J. Singh, S.-W. Lian, *et al.*, “Room-temperature intrinsic ferromagnetism in epitaxial CrTe_2 ultrathin films,” *Nature Communications* **12**, 1–9 (2021).
 - [24] M. Bonilla, S. Kolekar, Y. Ma, H. C. Diaz, V. Kalappattil, R. Das, T. Eggers, H. R. Gutierrez, M.-H. Phan, and M. Batzill, “Strong room-temperature ferromagnetism in VSe_2 monolayers on van der Waals substrates,” *Nature Nanotechnology* **13**, 289–293 (2018).
 - [25] J. Li, B. Zhao, P. Chen, R. Wu, B. Li, Q. Xia, G. Guo, J. Luo, K. Zang, Z. Zhang, *et al.*, “Synthesis of ultrathin metallic MTe_2 ($\text{M} = \text{V}, \text{Nb}, \text{Ta}$) single-crystalline nanoplates,” *Advanced Materials* **30**, 1801043 (2018).
 - [26] X. Zhang, B. Wang, Y. Guo, Y. Zhang, Y. Chen, and J. Wang, “High curie temperature and intrinsic ferromagnetic half-metallicity in two-dimensional Cr_3X_4 ($\text{X} = \text{S}, \text{Se}, \text{Te}$) nanosheets,” *Nanoscale Horizons* **4**, 859–866 (2019).
 - [27] K.-Z. Du, X.-Z. Wang, Y. Liu, P. Hu, M. I. B. Utama, C. K. Gan, Q. Xiong, and C. Kloc, “Weak van der Waals stacking, wide-range band gap, and Raman study on ultrathin layers of metal phosphorus trichalcogenides,” *ACS Nano* **10**, 1738–1743 (2016).
 - [28] Y. Deng, Y. Yu, Y. Song, J. Zhang, N. Z. Wang, Z. Sun, Y. Yi, Y. Z. Wu, S. Wu, J. Zhu, *et al.*, “Gate-tunable room-temperature ferromagnetism in two-dimensional Fe_3GeTe_2 ,” *Nature* **563**, 94–99 (2018).
 - [29] Z. Fei, B. Huang, P. Malinowski, W. Wang, T. Song, J. Sanchez, W. Yao, D. Xiao, X. Zhu, A. F. May, *et al.*, “Two-dimensional itinerant ferromagnetism in atomically thin Fe_3GeTe_2 ,” *Nature Materials* **17**, 778–782 (2018).

- [30] J. Seo, D. Y. Kim, E. S. An, K. Kim, G.-Y. Kim, S.-Y. Hwang, D. W. Kim, B. G. Jang, H. Kim, G. Eom, *et al.*, “Nearly room temperature ferromagnetism in a magnetic metal-rich van der Waals metal,” *Science Advances* **6**, eaay8912 (2020).
- [31] A. F. May, D. Ovchinnikov, Q. Zheng, R. Hermann, S. Calder, B. Huang, Z. Fei, Y. Liu, X. Xu, and M. A. McGuire, “Ferromagnetism near room temperature in the cleavable van der Waals crystal Fe_5GeTe_2 ,” *ACS Nano* **13**, 4436–4442 (2019).
- [32] Y. Deng, Y. Yu, M. Z. Shi, Z. Guo, Z. Xu, J. Wang, X. H. Chen, and Y. Zhang, “Quantum anomalous Hall effect in intrinsic magnetic topological insulator MnBi_2Te_4 ,” *Science* **367**, 895–900 (2020).
- [33] Z. Jiang, P. Wang, J. Xing, X. Jiang, and J. Zhao, “Screening and design of novel 2D ferromagnetic materials with high curie temperature above room temperature,” *ACS Applied Materials & Interfaces* **10**, 39032–39039 (2018).
- [34] Z. Li, D.-H. Xu, X. Li, H.-J. Liao, X. Xi, Y.-C. Yu, and W. Wang, “Anomalous spin dynamics in a two-dimensional magnet induced by anisotropic critical fluctuations,” *Physical Review B* **106**, 054427 (2022).
- [35] D. J. O’Hara, T. Zhu, A. H. Trout, A. S. Ahmed, Y. K. Luo, C. H. Lee, M. R. Brenner, S. Rajan, J. A. Gupta, D. W. McComb, *et al.*, “Room temperature intrinsic ferromagnetism in epitaxial manganese selenide films in the monolayer limit,” *Nano Letters* **18**, 3125–3131 (2018).
- [36] P. Park, K. Park, T. Kim, Y. Kousaka, K. H. Lee, T. Perring, J. Jeong, U. Stuhr, J. Akimitsu, M. Kenzelmann, *et al.*, “Momentum-dependent magnon lifetime in the metallic noncollinear triangular antiferromagnet CrB_2 ,” *Physical Review Letters* **125**, 027202 (2020).
- [37] S. Zhang, R. Xu, N. Luo, and X. Zou, “Two-dimensional magnetic materials: structures, properties and external controls,” *Nanoscale* **13**, 1398–1424 (2021).
- [38] X. Jiang, Q. Liu, J. Xing, N. Liu, Y. Guo, Z. Liu, and J. Zhao, “Recent progress on 2D magnets: Fundamental mechanism, structural design and modification,” *Applied Physics Reviews* **8**, 031305 (2021).
- [39] H. Xu, S. Xu, X. Xu, J. Zhuang, W. Hao, and Y. Du, “Recent advances in two-dimensional van der Waals magnets,” *Microstructures* **2**, 2022011 (2022).
- [40] Q. H. Wang, A. Bedoya-Pinto, M. Blei, A. H. Dismukes, A. Hamo, S. Jenkins, M. Koperski, Y. Liu, Q.-C. Sun, E. J. Telford, *et al.*, “The magnetic genome of two-dimensional van der Waals materials,” *ACS Nano* **16**, 6960–7079 (2022).
- [41] M. A. McGuire, H. Dixit, V. R. Cooper, and B. C. Sales, “Coupling of crystal structure and magnetism in the layered, ferromagnetic insulator CrI_3 ,” *Chemistry of Materials* **27**, 612–620 (2015).
- [42] T. Song, X. Cai, M. W.-Y. Tu, X. Zhang, B. Huang, N. P. Wilson, K. L. Seyler, L. Zhu, T. Taniguchi, K. Watanabe, *et al.*, “Giant tunneling magnetoresistance in spin-filter van der Waals heterostructures,” *Science* **360**, 1214–1218 (2018).
- [43] D. R. Klein, D. MacNeill, J. L. Lado, D. Soriano, E. Navarro-Moratalla, K. Watanabe, T. Taniguchi, S. Manni, P. Canfield, J. Fernández-Rossier, *et al.*, “Probing magnetism in 2D van der Waals crystalline insulators via electron tunneling,” *Science* **360**, 1218–1222 (2018).
- [44] H. H. Kim, B. Yang, T. Patel, F. Sfigakis, C. Li, S. Tian, H. Lei, and A. W. Tsen, “One million percent tunnel magnetoresistance in a magnetic van der Waals heterostructure,” *Nano Letters* **18**, 4885–4890 (2018).
- [45] Z. Wang, I. Gutiérrez-Lezama, N. Ubrig, M. Kroner, M. Gibertini, T. Taniguchi, K. Watanabe, A. Imamoğlu, E. Gianini, and A. F. Morpurgo, “Very large tunneling magnetoresistance in layered magnetic semiconductor CrI_3 ,” *Nature Communications* **9**, 1–8 (2018).
- [46] B. Huang, G. Clark, D. R. Klein, D. MacNeill, E. Navarro-Moratalla, K. L. Seyler, N. Wilson, M. A. McGuire, D. H. Cobden, D. Xiao, *et al.*, “Electrical control of 2D magnetism in bilayer CrI_3 ,” *Nature Nanotechnology* **13**, 544–548 (2018).
- [47] S. Jiang, J. Shan, and K. F. Mak, “Electric-field switching of two-dimensional van der Waals magnets,” *Nature Materials* **17**, 406–410 (2018).
- [48] S. Jiang, L. Li, Z. Wang, K. F. Mak, and J. Shan, “Controlling magnetism in 2D CrI_3 by electrostatic doping,” *Nature Nanotechnology* **13**, 549–553 (2018).
- [49] T. Li, S. Jiang, N. Sivadas, Z. Wang, Y. Xu, D. Weber, J. E. Goldberger, K. Watanabe, T. Taniguchi, C. J. Fennie, *et al.*, “Pressure-controlled interlayer magnetism in atomically thin CrI_3 ,” *Nature Materials* **18**, 1303–1308 (2019).
- [50] T. Song, Z. Fei, M. Yankowitz, Z. Lin, Q. Jiang, K. Hwangbo, Q. Zhang, B. Sun, T. Taniguchi, K. Watanabe, *et al.*, “Switching 2D magnetic states via pressure tuning of layer stacking,” *Nature Materials* **18**, 1298–1302 (2019).
- [51] K. S. Burch, D. Mandrus, and J.-G. Park, “Magnetism in two-dimensional van der Waals materials,” *Nature* **563**, 47–52 (2018).
- [52] M. Gibertini, M. Koperski, A. F. Morpurgo, and K. S. Novoselov, “Magnetic 2D materials and heterostructures,” *Nature Nanotechnology* **14**, 408–419 (2019).
- [53] C. Gong and X. Zhang, “Two-dimensional magnetic crystals and emergent heterostructure devices,” *Science* **363**, eaav4450 (2019).
- [54] K. F. Mak, J. Shan, and D. C. Ralph, “Probing and controlling magnetic states in 2D layered magnetic materials,” *Nature Reviews Physics* **1**, 646–661 (2019).
- [55] D. L. Cortie, G. L. Causer, K. C. Rule, H. Fritzsche, W. Kreuzpaintner, and F. Klose, “Two-dimensional magnets: forgotten history and recent progress towards spintronic applications,” *Advanced Functional Materials* **30**, 1901414 (2020).
- [56] J. F. Sierra, J. Fabian, R. K. Kawakami, S. Roche, and S. O. Valenzuela, “Van der Waals heterostructures for spintronics and opto-spintronics,” *Nature Nanotechnology* **16**, 856–868 (2021).
- [57] M. Och, M.-B. Martin, B. Dlubak, P. Seneor, and C. Mattevi, “Synthesis of emerging 2D layered magnetic materials,” *Nanoscale* **13**, 2157–2180 (2021).
- [58] Y. Yao, X. Zhan, M. G. Sendeku, P. Yu, F. T. Dajan, C. Zhu, N. Li, J. Wang, F. Wang, Z. Wang, *et al.*, “Recent progress on emergent two-dimensional magnets and heterostructures,” *Nanotechnology* **32**, 472001 (2021).

- [59] H. Kurebayashi, J. H. Garcia, S. Khan, J. Sinova, and S. Roche, “Magnetism, symmetry and spin transport in van der Waals layered systems,” *Nature Reviews Physics* **4**, 150–166 (2022).
- [60] X. Wang, K. Du, Y. Y. F. Liu, P. Hu, J. Zhang, Q. Zhang, M. H. S. Owen, X. Lu, C. K. Gan, P. Sengupta, *et al.*, “Raman spectroscopy of atomically thin two-dimensional magnetic iron phosphorus trisulfide (FePS₃) crystals,” *2D Materials* **3**, 031009 (2016).
- [61] W. Jin, H. H. Kim, Z. Ye, S. Li, P. Rezaie, F. Diaz, S. Siddiq, E. Wauer, B. Yang, C. Li, *et al.*, “Raman fingerprint of two terahertz spin wave branches in a two-dimensional honeycomb Ising ferromagnet,” *Nature Communications* **9**, 5122 (2018).
- [62] Y. Zhang, X. Wu, B. Lyu, M. Wu, S. Zhao, J. Chen, M. Jia, C. Zhang, L. Wang, X. Wang, *et al.*, “Magnetic order-induced polarization anomaly of Raman scattering in 2D magnet CrI₃,” *Nano Letters* **20**, 729–734 (2019).
- [63] K. Kim, J.-U. Lee, and H. Cheong, “Raman spectroscopy of two-dimensional magnetic van der Waals materials,” *Nanotechnology* **30**, 452001 (2019).
- [64] A. McCreary, T. T. Mai, F. G. Utermohlen, J. R. Simpson, K. F. Garrity, X. Feng, D. Shcherbakov, Y. Zhu, J. Hu, D. Weber, *et al.*, “Distinct magneto-Raman signatures of spin-flip phase transitions in CrI₃,” *Nature Communications* **11**, 3879 (2020).
- [65] A. McCreary, J. R. Simpson, T. T. Mai, R. D. McMichael, J. E. Douglas, N. Butch, C. Dennis, R. V. Aguilar, and A. R. H. Walker, “Quasi-two-dimensional magnon identification in antiferromagnetic FePS₃ via magneto-Raman spectroscopy,” *Physical Review B* **101**, 064416 (2020).
- [66] B. Huang, J. Cenker, X. Zhang, E. L. Ray, T. Song, T. Taniguchi, K. Watanabe, M. A. McGuire, D. Xiao, and X. Xu, “Tuning inelastic light scattering via symmetry control in the two-dimensional magnet CrI₃,” *Nature Nanotechnology* **15**, 212–216 (2020).
- [67] S. Li, Z. Ye, X. Luo, G. Ye, H. H. Kim, B. Yang, S. Tian, C. Li, H. Lei, A. W. Tsen, *et al.*, “Magnetic-field-induced quantum phase transitions in a van der Waals magnet,” *Physical Review X* **10**, 011075 (2020).
- [68] X. Guo, W. Jin, Z. Ye, G. Ye, H. Xie, B. Yang, H. H. Kim, S. Yan, Y. Fu, S. Tian, *et al.*, “Structural monoclinicity and its coupling to layered magnetism in few-layer CrI₃,” *ACS Nano* **15**, 10444–10450 (2021).
- [69] Y.-J. Sun, S.-M. Pang, and J. Zhang, “Review of Raman spectroscopy of two-dimensional magnetic van der Waals materials,” *Chinese Physics B* **30**, 117104 (2021).
- [70] X. Wang, J. Cao, H. Li, Z. Lu, A. Cohen, A. Haldar, H. Kitadai, Q. Tan, K. S. Burch, D. Smirnov, *et al.*, “Electronic Raman scattering in the 2D antiferromagnet NiPS₃,” *Science Advances* **8**, eabl7707 (2022).
- [71] K. L. Seyler, D. Zhong, D. R. Klein, S. Gao, X. Zhang, B. Huang, E. Navarro-Moratalla, L. Yang, D. H. Cobden, M. A. McGuire, *et al.*, “Ligand-field helical luminescence in a 2D ferromagnetic insulator,” *Nature Physics* **14**, 277–281 (2018).
- [72] M. Wu, Z. Li, T. Cao, and S. G. Louie, “Physical origin of giant excitonic and magneto-optical responses in two-dimensional ferromagnetic insulators,” *Nature Communications* **10**, 2371 (2019).
- [73] W. Jin, H. H. Kim, Z. Ye, G. Ye, L. Rojas, X. Luo, B. Yang, F. Yin, J. S. A. Horng, S. Tian, *et al.*, “Observation of the polaronic character of excitons in a two-dimensional semiconducting magnet CrI₃,” *Nature Communications* **11**, 4780 (2020).
- [74] M. Wu, Z. Li, and S. G. Louie, “Optical and magneto-optical properties of ferromagnetic monolayer CrBr₃: A first-principles *GW* and *GW* plus Bethe-Salpeter equation study,” *Physical Review Materials* **6**, 014008 (2022).
- [75] Z. Frait and D. Fraitova, “Spin-wave resonance in metals,” in *Modern Problems in Condensed Matter Sciences*, Vol. 22 (Elsevier, 1988) pp. 1–65.
- [76] B. Heinrich and J. Cochran, “Ultrathin metallic magnetic films: magnetic anisotropies and exchange interactions,” *Advances in Physics* **42**, 523–639 (1993).
- [77] M. Farle, “Ferromagnetic resonance of ultrathin metallic layers,” *Reports on Progress in Physics* **61**, 755 (1998).
- [78] I. S. Maksymov and M. Kostylev, “Broadband stripline ferromagnetic resonance spectroscopy of ferromagnetic films, multilayers and nanostructures,” *Physica E: Low-dimensional Systems and Nanostructures* **69**, 253–293 (2015).
- [79] S. V. Vonsovskii, *Ferromagnetic resonance: the phenomenon of resonant absorption of a high-frequency magnetic field in ferromagnetic substances* (Pergamon, Oxford, 2016).
- [80] D. S. Schmool, D. Markó, K.-W. Lin, A. Hierro-Rodríguez, C. Quirós, J. Díaz, L. M. Álvarez-Prado, and J.-C. Wu, “Ferromagnetic resonance studies in magnetic nanosystems,” *Magnetochemistry* **7**, 126 (2021).
- [81] C. Kittel, “On the theory of ferromagnetic resonance absorption,” *Physical Review* **73**, 155 (1948).
- [82] T. Phillips and H. Rosenberg, “Spin waves in ferromagnets,” *Reports on Progress in Physics* **29**, 285 (1966).
- [83] S. Barnes, “Theory of electron spin resonance of magnetic ions in metals,” *Advances in Physics* **30**, 801–938 (1981).
- [84] T. Gilbert, “A lagrangian formulation of the gyromagnetic equation of the magnetization field,” *Physical Review* **100**, 1243 (1955).
- [85] M. Lakshmanan, “The fascinating world of the Landau–Lifshitz–Gilbert equation: an overview,” *Philosophical Transactions of the Royal Society A: Mathematical, Physical and Engineering Sciences* **369**, 1280–1300 (2011).
- [86] M. Harder, Z. Cao, Y. Gui, X. Fan, and C.-M. Hu, “Analysis of the line shape of electrically detected ferromagnetic resonance,” *Physical Review B* **84**, 054423 (2011).
- [87] J. Artman, “Ferromagnetic resonance in metal single crystals,” *Physical Review* **105**, 74 (1957).
- [88] L. Baselgia, M. Warden, F. Waldner, S. L. Hutton, J. E. Drumheller, Y. He, P. Wigen, and M. Maryško, “Derivation of the resonance frequency from the free energy of ferromagnets,” *Physical Review B* **38**, 2237 (1988).
- [89] J. Zeisner, K. Mehawat, A. Alfonsov, M. Roslova, T. Doert, A. Isaeva, B. Büchner, and V. Kataev, “Electron spin resonance and ferromagnetic resonance spectroscopy in the high-field phase of the van der Waals magnet CrCl₃,” *Physical*

Review Materials **4**, 064406 (2020).

- [90] I. Lee, F. G. Utermohlen, D. Weber, K. Hwang, C. Zhang, J. van Tol, J. E. Goldberger, N. Trivedi, and P. C. Hammel, “Fundamental spin interactions underlying the magnetic anisotropy in the Kitaev ferromagnet CrI_3 ,” *Physical Review Letters* **124**, 017201 (2020).
- [91] S. Acharya, D. Pashov, B. Cunningham, A. N. Rudenko, M. Rösner, M. Grüning, M. van Schilfgaarde, and M. I. Katsnelson, “Electronic structure of chromium trihalides beyond density functional theory,” *Physical Review B* **104**, 155109 (2021).
- [92] B. Zhang, Y. Zeng, Z.-J. Zhao, D.-P. Qiu, T. Zhang, and Y.-L. Hou, “Magnetic two-dimensional chromium trihalides: structure, properties and modulation,” *Rare Metals* **41**, 2921–2942 (2022).
- [93] J. Cable, M. Wilkinson, and E. Wollan, “Neutron diffraction investigation of antiferromagnetism in CrCl_3 ,” *Journal of Physics and Chemistry of Solids* **19**, 29–34 (1961).
- [94] M. A. McGuire, G. Clark, K. Santosh, W. M. Chance, G. E. Jellison Jr, V. R. Cooper, X. Xu, and B. C. Sales, “Magnetic behavior and spin-lattice coupling in cleavable van der Waals layered CrCl_3 crystals,” *Physical Review Materials* **1**, 014001 (2017).
- [95] G. Bastien, M. Roslova, M. Haghighi, K. Mehlaawat, J. Hunger, A. Isaeva, T. Doert, M. Vojta, B. Büchner, and A. Wolter, “Spin-glass state and reversed magnetic anisotropy induced by Cr doping in the Kitaev magnet $\alpha\text{-RuCl}_3$,” *Physical Review B* **99**, 214410 (2019).
- [96] S. Khan, C. Zollitsch, D. Arroo, H. Cheng, I. Verzhbitskiy, A. Sud, Y. Feng, G. Eda, and H. Kurebayashi, “Spin dynamics study in layered van der Waals single-crystal $\text{Cr}_2\text{Ge}_2\text{Te}_6$,” *Physical Review B* **100**, 134437 (2019).
- [97] J. Dillon Jr and C. Olson, “Magnetization, resonance, and optical properties of the ferromagnet CrI_3 ,” *Journal of Applied Physics* **36**, 1259–1260 (1965).
- [98] J. L. Lado and J. Fernández-Rossier, “On the origin of magnetic anisotropy in two dimensional CrI_3 ,” *2D Materials* **4**, 035002 (2017).
- [99] D. A. Wahab, M. Augustin, S. M. Valero, W. Kuang, S. Jenkins, E. Coronado, I. V. Grigorieva, I. J. Vera-Marun, E. Navarro-Moratalla, R. F. L. Evans, K. S. Novoselov, and E. J. G. Santos, “Quantum rescaling, domain metastability, and hybrid domain-walls in 2d CrI_3 magnets,” *Adv. Mater.* **33**, 2004138 (2021), <https://onlinelibrary.wiley.com/doi/pdf/10.1002/adma.202004138>.
- [100] A. Kartsev, M. Augustin, R. F. L. Evans, K. S. Novoselov, and E. J. G. Santos, “Biquadratic exchange interactions in two-dimensional magnets,” *npj Comput. Mater.* **6**, 150 (2020).
- [101] C. Xu, J. Feng, H. Xiang, and L. Bellaiche, “Interplay between Kitaev interaction and single ion anisotropy in ferromagnetic CrI_3 and CrGeTe_3 monolayers,” *npj Computational Materials* **4**, 1–6 (2018).
- [102] D. G. Joshi, “Topological excitations in the ferromagnetic Kitaev-Heisenberg model,” *Physical Review B* **98**, 060405 (2018).
- [103] M. Deb and A. K. Ghosh, “Topological phases of higher Chern numbers in Kitaev-Heisenberg ferromagnet with further-neighbor interactions,” *Journal of Physics: Condensed Matter* **31**, 345601 (2019).
- [104] L. Chen, J.-H. Chung, T. Chen, C. Duan, A. Schneidewind, I. Radelytskyi, D. J. Voneshen, R. A. Ewings, M. B. Stone, A. I. Kolesnikov, *et al.*, “Magnetic anisotropy in ferromagnetic CrI_3 ,” *Physical Review B* **101**, 134418 (2020).
- [105] L. Chen, J.-H. Chung, T. Chen, C. Duan, A. Schneidewind, I. Radelytskyi, D. J. Voneshen, R. A. Ewings, M. B. Stone, A. I. Kolesnikov, B. Winn, S. Chi, R. A. Mole, D. H. Yu, B. Gao, and P. Dai, “Magnetic anisotropy in ferromagnetic CrI_3 ,” *Phys. Rev. B* **101**, 134418 (2020).
- [106] L. Chen, J.-H. Chung, B. Gao, T. Chen, M. B. Stone, A. I. Kolesnikov, Q. Huang, and P. Dai, “Topological spin excitations in honeycomb ferromagnet CrI_3 ,” *Phys. Rev. X* **8**, 041028 (2018).
- [107] L. Chen, J.-H. Chung, M. B. Stone, A. I. Kolesnikov, B. Winn, V. O. Garlea, D. L. Abernathy, B. Gao, M. Augustin, E. J. G. Santos, and P. Dai, “Magnetic field effect on topological spin excitations in CrI_3 ,” *Phys. Rev. X* **11**, 031047 (2021).
- [108] L. Alahmed, B. Nepal, J. Macy, W. Zheng, B. Casas, A. Sapkota, N. Jones, A. R. Mazza, M. Brahlek, W. Jin, *et al.*, “Magnetism and spin dynamics in room-temperature van der Waals magnet Fe_5GeTe_2 ,” *2D Materials* **8**, 045030 (2021).
- [109] V. Korenman, J. Murray, and R. Prange, “Local-band theory of itinerant ferromagnetism. II. spin waves,” *Physical Review B* **16**, 4048 (1977).
- [110] H. Capellmann, “Theory of itinerant ferromagnetism in the 3-d transition metals,” *Zeitschrift für Physik B Condensed Matter* **34**, 29–35 (1979).
- [111] T. Moriya, “Recent progress in the theory of itinerant electron magnetism,” *Journal of Magnetism and Magnetic Materials* **14**, 1–46 (1979).
- [112] T. Moriya, “Theory of itinerant electron magnetism,” *Journal of Magnetism and Magnetic Materials* **100**, 261–271 (1991).
- [113] H. Zhang, R. Chen, K. Zhai, X. Chen, L. Caretta, X. Huang, R. V. Chopdekar, J. Cao, J. Sun, J. Yao, *et al.*, “Itinerant ferromagnetism in van der Waals $\text{Fe}_{5-x}\text{GeTe}_2$ crystals above room temperature,” *Physical Review B* **102**, 064417 (2020).
- [114] S. Mondal, N. Khan, S. M. Mishra, B. Satpati, and P. Mandal, “Critical behavior in the van der Waals itinerant ferromagnet Fe_4GeTe_2 ,” *Physical Review B* **104**, 094405 (2021).
- [115] X. Wu, L. Lei, Q. Yin, N.-N. Zhao, M. Li, Z. Wang, Q. Liu, W. Song, H. Ma, P. Ding, *et al.*, “Direct observation of competition between charge order and itinerant ferromagnetism in the van der Waals crystal $\text{Fe}_{5-x}\text{GeTe}_2$,” *Physical Review B* **104**, 165101 (2021).
- [116] S. Ershadrad, S. Ghosh, D. Wang, Y. Kvashnin, and B. Sanyal, “Unusual magnetic features in two-dimensional Fe_5GeTe_2 induced by structural reconstructions,” *The Journal of Physical Chemistry Letters* **13**, 4877–4883 (2022).

- [117] M. Joe, U. Yang, and C. Lee, “First-principles study of ferromagnetic metal Fe_5GeTe_2 ,” *Nano Materials Science* **1**, 299–303 (2019).
- [118] K. Yamagami, Y. Fujisawa, B. Driesen, C.-H. Hsu, K. Kawaguchi, H. Tanaka, T. Kondo, Y. Zhang, H. Wadati, K. Araki, *et al.*, “Itinerant ferromagnetism mediated by giant spin polarization of the metallic ligand band in the van der Waals magnet Fe_5GeTe_2 ,” *Physical Review B* **103**, L060403 (2021).
- [119] X. Shen, H. Chen, Y. Li, H. Xia, F. Zeng, J. Xu, H. Y. Kwon, Y. Ji, C. Won, W. Zhang, *et al.*, “Multi-domain ferromagnetic resonance in magnetic van der Waals crystals CrI_3 and CrBr_3 ,” *Journal of Magnetism and Magnetic Materials* **528**, 167772 (2021).
- [120] K. Nagata, “Short range order effects on EPR frequencies in antiferromagnets,” *Physica B+C* **86**, 1283–1284 (1977).
- [121] K. Nagata, I. Yamamoto, H. Takano, and Y. Yokozawa, “EPR g-shift and anisotropic magnetic susceptibility in K_2MnF_4 ,” *Journal of the Physical Society of Japan* **43**, 857–861 (1977).
- [122] D. Abdul-Wahab, E. Iacocca, R. F. L. Evans, A. Bedoya-Pinto, S. Parkin, K. S. Novoselov, and E. J. G. Santos, “Domain wall dynamics in two-dimensional van der Waals ferromagnets,” *Appl. Phys. Rev.* **8**, 041411 (2021).
- [123] D. MacNeill, J. T. Hou, D. R. Klein, P. Zhang, P. Jarillo-Herrero, and L. Liu, “Gigahertz frequency antiferromagnetic resonance and strong magnon-magnon coupling in the layered crystal CrCl_3 ,” *Physical Review Letters* **123**, 047204 (2019).
- [124] H. Wang, V. Eyert, and U. Schwingenschlögl, “Electronic structure and magnetic ordering of the semiconducting chromium trihalides CrCl_3 , CrBr_3 , and CrI_3 ,” *Journal of Physics: Condensed Matter* **23**, 116003 (2011).
- [125] Z. Wang, M. Gibertini, D. Dumcenco, T. Taniguchi, K. Watanabe, E. Giannini, and A. F. Morpurgo, “Determining the phase diagram of atomically thin layered antiferromagnet CrCl_3 ,” *Nature Nanotechnology* **14**, 1116–1122 (2019).
- [126] A. Kirilyuk, A. V. Kimel, and T. Rasing, “Ultrafast optical manipulation of magnetic order,” *Reviews of Modern Physics* **82**, 2731 (2010).
- [127] Y. Hashimoto, S. Daimon, R. Iguchi, Y. Oikawa, K. Shen, K. Sato, D. Bossini, Y. Tabuchi, T. Satoh, B. Hillebrands, *et al.*, “All-optical observation and reconstruction of spin wave dispersion,” *Nature Communications* **8**, 1–6 (2017).
- [128] F. B. Mushenok, R. Dost, C. S. Davies, D. A. Allwood, B. J. Inkson, G. Hrkac, and V. V. Kruglyak, “Broadband conversion of microwaves into propagating spin waves in patterned magnetic structures,” *Applied Physics Letters* **111**, 042404 (2017).
- [129] Y. Li, F. Zeng, H. Saglam, J. Sklenar, J. E. Pearson, T. Sebastian, Y. Wu, A. Hoffmann, and W. Zhang, “Optical detection of phase-resolved ferromagnetic resonance in epitaxial FeCo thin films,” *IEEE Transactions on Magnetics* **55**, 1–5 (2019).
- [130] M. Deb, E. Popova, M. Hehn, N. Keller, S. Petit-Watlot, M. Bargheer, S. Mangin, and G. Malinowski, “Damping of standing spin waves in bismuth-substituted yttrium iron garnet as seen via the time-resolved magneto-optical Kerr effect,” *Physical Review Applied* **12**, 044006 (2019).
- [131] J. Zhu, X. Wu, D. M. Lattery, W. Zheng, and X. Wang, “The ultrafast laser pump-probe technique for thermal characterization of materials with micro/nanostructures,” *Nanoscale and Microscale Thermophysical Engineering* **21**, 177–198 (2017).
- [132] D. Huang, D. Lattery, and X. Wang, “Materials engineering enabled by time-resolved magneto-optical Kerr effect for spintronic applications,” *ACS Applied Electronic Materials* **3**, 119–127 (2020).
- [133] T. Zhang, Y. Chen, Y. Li, Z. Guo, Z. Wang, Z. Han, W. He, and J. Zhang, “Laser-induced magnetization dynamics in a van der Waals ferromagnetic $\text{Cr}_2\text{Ge}_2\text{Te}_6$ nanoflake,” *Applied Physics Letters* **116**, 223103 (2020).
- [134] X.-X. Zhang, L. Li, D. Weber, J. Goldberger, K. F. Mak, and J. Shan, “Gate-tunable spin waves in antiferromagnetic atomic bilayers,” *Nature Materials* **19**, 838–842 (2020).
- [135] S. Iihama, S. Mizukami, H. Naganuma, M. Oogane, Y. Ando, and T. Miyazaki, “Gilbert damping constants of $\text{Ta}/\text{CoFeB}/\text{MgO}$ (Ta) thin films measured by optical detection of precessional magnetization dynamics,” *Physical Review B* **89**, 174416 (2014).
- [136] J. Pelzl, R. Meckenstock, D. Spoddig, F. Schreiber, J. Pflaum, and Z. Frait, “Spin-orbit-coupling effects on g-value and damping factor of the ferromagnetic resonance in Co and Fe films,” *Journal of Physics: Condensed Matter* **15**, S451 (2003).
- [137] L. Ni, Z. Chen, W. Li, X. Lu, Y. Yan, L. Zhang, C. Yan, Y. Chen, Y. Gu, Y. Li, *et al.*, “Magnetic dynamics of two-dimensional itinerant ferromagnet Fe_3GeTe_2 ,” *Chinese Physics B* **30**, 097501 (2021).
- [138] K. Lee, A. H. Dismukes, E. J. Telford, R. A. Wiscons, J. Wang, X. Xu, C. Nuckolls, C. R. Dean, X. Roy, and X. Zhu, “Magnetic order and symmetry in the 2D semiconductor CrSBr ,” *Nano Letters* **21**, 3511–3517 (2021).
- [139] E. J. Telford, A. H. Dismukes, K. Lee, M. Cheng, A. Wieteska, A. K. Bartholomew, Y.-S. Chen, X. Xu, A. N. Pasupathy, X. Zhu, *et al.*, “Layered antiferromagnetism induces large negative magnetoresistance in the van der Waals semiconductor CrSBr ,” *Advanced Materials* **32**, 2003240 (2020).
- [140] N. P. Wilson, K. Lee, J. Cenker, K. Xie, A. H. Dismukes, E. J. Telford, J. Fonseca, S. Sivakumar, C. Dean, T. Cao, *et al.*, “Interlayer electronic coupling on demand in a 2D magnetic semiconductor,” *Nature Materials* **20**, 1657–1662 (2021).
- [141] Y. J. Bae, J. Wang, A. Scheie, J. Xu, D. G. Chica, G. M. Diederich, J. Cenker, M. E. Ziebel, Y. Bai, H. Ren, *et al.*, “Exciton-coupled coherent magnons in a 2D semiconductor,” *Nature* **609**, 282–286 (2022).
- [142] L. Lüer, C. Gadermaier, J. Crochet, T. Hertel, D. Brida, and G. Lanzani, “Coherent phonon dynamics in semiconducting carbon nanotubes: A quantitative study of electron-phonon coupling,” *Physical Review Letters* **102**, 127401 (2009).
- [143] A. T. Kumar, F. Rosca, A. Widom, and P. M. Champion, “Investigations of amplitude and phase excitation profiles in femtosecond coherence spectroscopy,” *The Journal of Chemical Physics* **114**, 701–724 (2001).
- [144] Q. Chen, J. Liang, B. Fang, Y. Zhu, J. Wang, W. Lv, W. Lv, J. Cai, Z. Huang, Y. Zhai, *et al.*, “Proximity effect of a two-dimensional van der Waals magnet Fe_3GeTe_2 on nickel films,” *Nanoscale* **13**, 14688–14693 (2021).

- [145] A. Mellnik, J. Lee, A. Richardella, J. Grab, P. Mintun, M. H. Fischer, A. Vaezi, A. Manchon, E.-A. Kim, N. Samarth, *et al.*, “Spin-transfer torque generated by a topological insulator,” *Nature* **511**, 449–451 (2014).
- [146] H. Zhang, Y.-T. Shao, R. Chen, X. Chen, S. Susarla, D. Raftrey, J. T. Reichanadter, L. Caretta, X. Huang, N. S. Settineri, Z. Chen, J. Zhou, E. Bourret-Courchesne, P. Ercius, J. Yao, P. Fischer, J. B. Neaton, D. A. Muller, R. J. Birgeneau, and R. Ramesh, “A room temperature polar magnetic metal,” *Physical Review Materials* **6**, 044403 (2022).
- [147] A. Scheie, M. Ziebel, D. G. Chica, Y. J. Bae, X. Wang, A. I. Kolesnikov, X. Zhu, and X. Roy, “Spin waves and magnetic exchange Hamiltonian in CrSBr,” *Advanced Science*, 2202467 (2022).
- [148] D. C. Ralph and M. D. Stiles, “Spin transfer torques,” *Journal of Magnetism and Magnetic Materials* **320**, 1190–1216 (2008).
- [149] E. Chen, D. Apalkov, Z. Diao, A. Driskill-Smith, D. Druist, D. Lottis, V. Nikitin, X. Tang, S. Watts, S. Wang, *et al.*, “Advances and future prospects of spin-transfer torque random access memory,” *IEEE Transactions on Magnetics* **46**, 1873–1878 (2010).
- [150] T. Kawahara, K. Ito, R. Takemura, and H. Ohno, “Spin-transfer torque RAM technology: Review and prospect,” *Microelectronics Reliability* **52**, 613–627 (2012).
- [151] L. Thomas, G. Jan, J. Zhu, H. Liu, Y.-J. Lee, S. Le, R.-Y. Tong, K. Pi, Y.-J. Wang, D. Shen, *et al.*, “Perpendicular spin transfer torque magnetic random access memories with high spin torque efficiency and thermal stability for embedded applications,” *Journal of Applied Physics* **115**, 172615 (2014).
- [152] N. Locatelli, V. Cros, and J. Grollier, “Spin-torque building blocks,” *Nature Materials* **13**, 11–20 (2014).
- [153] X. Fong, Y. Kim, K. Yogendra, D. Fan, A. Sengupta, A. Raghunathan, and K. Roy, “Spin-transfer torque devices for logic and memory: Prospects and perspectives,” *IEEE Transactions on Computer-Aided Design of Integrated Circuits and Systems* **35**, 1–22 (2015).
- [154] S. Parkin and S.-H. Yang, “Memory on the racetrack,” *Nature Nanotechnology* **10**, 195–198 (2015).
- [155] J. Hirsch, “Spin Hall effect,” *Physical Review Letters* **83**, 1834 (1999).
- [156] Y. K. Kato, R. C. Myers, A. C. Gossard, and D. D. Awschalom, “Observation of the spin Hall effect in semiconductors,” *Science* **306**, 1910–1913 (2004).
- [157] S. O. Valenzuela and M. Tinkham, “Direct electronic measurement of the spin Hall effect,” *Nature* **442**, 176–179 (2006).
- [158] T. Kimura, Y. Otani, T. Sato, S. Takahashi, and S. Maekawa, “Room-temperature reversible spin Hall effect,” *Physical Review Letters* **98**, 156601 (2007).
- [159] J. Sinova, S. O. Valenzuela, J. Wunderlich, C. Back, and T. Jungwirth, “Spin Hall effects,” *Reviews of Modern Physics* **87**, 1213 (2015).
- [160] V. M. Edelstein, “Spin polarization of conduction electrons induced by electric current in two-dimensional asymmetric electron systems,” *Solid State Communications* **73**, 233–235 (1990).
- [161] S. D. Ganichev, E. Ivchenko, V. Bel’Kov, S. Tarasenko, M. Sollinger, D. Weiss, W. Wegscheider, and W. Prettl, “Spin-galvanic effect,” *Nature* **417**, 153–156 (2002).
- [162] J. Sánchez, L. Vila, G. Desfonds, S. Gambarelli, J. Attané, J. De Teresa, C. Magén, and A. Fert, “Spin-to-charge conversion using Rashba coupling at the interface between non-magnetic materials,” *Nature Communications* **4**, 1–7 (2013).
- [163] A. Manchon, H. C. Koo, J. Nitta, S. Frolov, and R. Duine, “New perspectives for Rashba spin–orbit coupling,” *Nature Materials* **14**, 871–882 (2015).
- [164] A. Hoffmann, “Spin Hall effects in metals,” *IEEE Transactions on Magnetics* **49**, 5172–5193 (2013).
- [165] H. Wang, C. Du, Y. Pu, R. Adur, P. C. Hammel, and F. Yang, “Scaling of spin Hall angle in 3d, 4d, and 5d metals from $\text{Y}_3\text{Fe}_5\text{O}_{12}$ /metal spin pumping,” *Physical Review Letters* **112**, 197201 (2014).
- [166] T. Horaguchi, M. Matsuo, and Y. Nozaki, “Highly accurate evaluation of spin-torque efficiency by measuring in-plane angular dependence of spin-torque ferromagnetic resonance,” *Journal of Magnetism and Magnetic Materials* **505**, 166727 (2020).
- [167] L. Liu, T. Moriyama, D. Ralph, and R. Buhrman, “Spin-torque ferromagnetic resonance induced by the spin Hall effect,” *Physical Review Letters* **106**, 036601 (2011).
- [168] Z.-K. Xie, Y. Li, Z.-Z. Gong, X. Yang, Y. Li, R. Sun, N. Li, Y.-B. Sun, J.-J. Zhao, Z.-H. Cheng, *et al.*, “Characterizing the magnetic interfacial coupling of the Fe/FeGe heterostructure by ferromagnetic resonance,” *ACS Applied Materials & Interfaces* **12**, 46908–46913 (2020).
- [169] H. Chang, P. Li, W. Zhang, T. Liu, A. Hoffmann, L. Deng, and M. Wu, “Nanometer-thick yttrium iron garnet films with extremely low damping,” *IEEE Magnetics Letters* **5**, 1–4 (2014).
- [170] P. Yu, X. Jin, J. Kudrnovský, D. Wang, and P. Bruno, “Curie temperatures of fcc and bcc nickel and permalloy: Supercell and Green’s function methods,” *Physical Review B* **77**, 054431 (2008).
- [171] D. D. Awschalom, C. R. Du, R. He, F. J. Heremans, A. Hoffmann, J. Hou, H. Kurebayashi, Y. Li, L. Liu, V. Novosad, J. Sklenar, S. E. Sullivan, D. Sun, H. Tang, V. Tyberkevych, C. Trevillian, A. W. Tsen, L. R. Weiss, W. Zhang, X. Zhang, L. Zhao, and C. W. Zollitsch, “Quantum engineering with hybrid magnonic systems and materials (invited paper),” *IEEE Transactions on Quantum Engineering* **2**, 1–36 (2021).
- [172] J. Sklenar and W. Zhang, “Self-hybridization and tunable magnon-magnon coupling in van der Waals synthetic magnets,” *Physical Review Applied* **15**, 044008 (2021).
- [173] T. Jeffrey, W. Zhang, and J. Sklenar, “Effect of dipolar interaction on exceptional points in synthetic layered magnets,” *Applied Physics Letters* **118**, 202401 (2021).
- [174] X.-G. Wang, G.-H. Guo, and J. Berakdar, “Steering magnonic dynamics and permeability at exceptional points in a parity–time symmetric waveguide,” *Nature Communications* **11**, 5663 (2020).

- [175] Y. Xiong, Y. Li, R. Bidthanapally, J. Sklenar, M. Hammami, S. Hall, X. Zhang, P. Li, J. E. Pearson, T. Sebastian, *et al.*, “Detecting phase-resolved magnetization dynamics by magneto-optic effects at 1550 nm wavelength,” *IEEE Transactions on Magnetics* **57**, 1–7 (2020).
- [176] C. W. Zollitsch, S. Khan, V. T. T. Nam, I. A. Verzhbitskiy, D. Sagkovits, J. O’Sullivan, O. W. Kennedy, M. Strungaru, E. J. Santos, J. J. Morton, *et al.*, “Probing spin dynamics of ultra-thin van der Waals magnets via photon-magnon coupling,” *arXiv preprint arXiv:2206.02460* (2022).
- [177] Y. Tabuchi, S. Ishino, A. Noguchi, T. Ishikawa, R. Yamazaki, K. Usami, and Y. Nakamura, “Quantum magnonics: The magnon meets the superconducting qubit,” *Comptes Rendus Physique* **17**, 729–739 (2016).
- [178] D. Lachance-Quirion, Y. Tabuchi, A. Gloppe, K. Usami, and Y. Nakamura, “Hybrid quantum systems based on magnonics,” *Applied Physics Express* **12**, 070101 (2019).
- [179] H. Yuan, Y. Cao, A. Kamra, R. A. Duine, and P. Yan, “Quantum magnonics: when magnon spintronics meets quantum information science,” *Physics Reports* **965**, 1–74 (2022).
- [180] S. Yoon, J. Liu, and R. D. McMichael, “Phase-resolved ferromagnetic resonance using a heterodyne detection method,” *Physical Review B* **93**, 144423 (2016).
- [181] Y. Li, H. Saglam, Z. Zhang, R. Bidthanapally, Y. Xiong, J. E. Pearson, V. Novosad, H. Qu, G. Srinivasan, A. Hoffmann, *et al.*, “Simultaneous optical and electrical spin-torque magnetometry with phase-sensitive detection of spin precession,” *Physical Review Applied* **11**, 034047 (2019).
- [182] Y. Xiong, Y. Li, M. Hammami, R. Bidthanapally, J. Sklenar, X. Zhang, H. Qu, G. Srinivasan, J. Pearson, A. Hoffmann, *et al.*, “Probing magnon–magnon coupling in exchange coupled $\text{Y}_3\text{Fe}_5\text{O}_{12}$ /Permalloy bilayers with magneto-optical effects,” *Scientific Reports* **10**, 12548 (2020).
- [183] Y. Li, F. Zeng, H. Saglam, J. Sklenar, J. E. Pearson, T. Sebastian, Y. Wu, A. Hoffmann, and W. Zhang, “Optical detection of phase-resolved ferromagnetic resonance in epitaxial FeCo thin films,” *IEEE Transactions on Magnetics* **55**, 1–5 (2019).
- [184] Y. Xiong, J. Inman, Z. Li, K. Xie, R. Bidthanapally, J. Sklenar, P. Li, S. Louis, V. Tyberkevych, H. Qu, *et al.*, “Tunable magnetically induced transparency spectra in magnon-magnon coupled $\text{Y}_3\text{Fe}_5\text{O}_{12}$ /Permalloy bilayers,” *Physical Review Applied* **17**, 044010 (2022).
- [185] J. Inman, Y. Xiong, R. Bidthanapally, S. Louis, V. Tyberkevych, H. Qu, J. Sklenar, V. Novosad, Y. Li, X. Zhang, *et al.*, “Hybrid magnonics for short-wavelength spin waves facilitated by a magnetic heterostructure,” *Physical Review Applied* **17**, 044034 (2022).
- [186] S. Mandal, L. N. Kapoor, S. Ghosh, J. Jesudasan, S. Manni, A. Thamizhavel, P. Raychaudhuri, V. Singh, and M. M. Deshmukh, “Coplanar cavity for strong coupling between photons and magnons in van der Waals antiferromagnet,” *Applied Physics Letters* **117**, 263101 (2020).
- [187] Q. Zhang, Y. Sun, Z. Lu, J. Guo, J. Xue, Y. Chen, Y. Tian, S. Yan, and L. Bai, “Zero-field magnon–photon coupling in antiferromagnet CrCl_3 ,” *Applied Physics Letters* **119**, 102402 (2021).
- [188] N. J. McLaughlin, C. Hu, M. Huang, S. Zhang, H. Lu, G. Q. Yan, H. Wang, Y. Tserkovnyak, N. Ni, and C. R. Du, “Quantum imaging of magnetic phase transitions and spin fluctuations in intrinsic magnetic topological nanoflakes,” *Nano Letters* **22**, 5810–5817 (2022).
- [189] L. McKenzie-Sell, J. Xie, C.-M. Lee, J. W. A. Robinson, C. Ciccirelli, and J. A. Haigh, “Low-impedance superconducting microwave resonators for strong coupling to small magnetic mode volumes,” *Physical Review B* **99**, 140414 (2019).
- [190] I. Gimeno, W. Kersten, M. C. Pallarés, P. Hermosilla, M. J. Martínez-Pérez, M. D. Jenkins, A. Angerer, C. Sánchez-Azqueta, D. Zueco, J. Majer, A. Lostao, and F. Luis, “Enhanced molecular spin-photon coupling at superconducting nanoconstrictions,” *ACS Nano* **14**, 8707–8715 (2020).
- [191] Y. Huang, Y.-H. Pan, R. Yang, L.-H. Bao, L. Meng, H.-L. Luo, Y.-Q. Cai, G.-D. Liu, W.-J. Zhao, Z. Zhou, L.-M. Wu, Z.-L. Zhu, M. Huang, L.-W. Liu, L. Liu, P. Cheng, K.-H. Wu, S.-B. Tian, C.-Z. Gu, Y.-G. Shi, Y.-F. Guo, Z. G. Cheng, J.-P. Hu, L. Zhao, G.-H. Yang, E. Sutter, P. Sutter, Y.-L. Wang, W. Ji, X.-J. Zhou, and H.-J. Gao, “Universal mechanical exfoliation of large-area 2D crystals,” *Nature Communications* **11**, 2453 (2020).
- [192] D. N. Basov, M. M. Fogler, and F. J. G. de Abajo, “Polaritons in van der Waals materials,” *Science* **354**, aag1992 (2016).
- [193] T. Low, A. Chaves, J. D. Caldwell, A. Kumar, N. X. Fang, P. Avouris, F. Heinz, Tony F. and Guinea, L. Martin-Moreno, and F. Koppens, “Polaritons in layered two-dimensional materials,” *Nature Materials* **16**, 182–194 (2017).
- [194] C. L. Degen, F. Reinhard, and P. Cappellaro, “Quantum sensing,” *Reviews of Modern Physics* **89**, 035002 (2017).
- [195] L. Thiel, Z. Wang, M. A. Tschudin, D. Rohner, I. Gutiérrez-Lezama, N. Ubrig, M. Gibertini, E. Giannini, A. F. Morpurgo, and P. Maletinsky, “Probing magnetism in 2D materials at the nanoscale with single-spin microscopy,” *Science* **364**, 973–976 (2019).
- [196] Q.-C. Sun, T. Song, E. Anderson, A. Brunner, J. Förster, T. Shalomayeva, T. Taniguchi, K. Watanabe, J. Gräfe, R. Stöhr, *et al.*, “Magnetic domains and domain wall pinning in atomically thin CrBr_3 revealed by nanoscale imaging,” *Nature Communications* **12**, 1–7 (2021).
- [197] D. A. Broadway, S. C. Scholten, C. Tan, N. Dontschuk, S. E. Lillie, B. C. Johnson, G. Zheng, Z. Wang, A. R. Oganov, S. Tian, *et al.*, “Imaging domain reversal in an ultrathin van der Waals ferromagnet,” *Advanced Materials* **32**, 2003314 (2020).
- [198] T. Song, Q.-C. Sun, E. Anderson, C. Wang, J. Qian, T. Taniguchi, K. Watanabe, M. A. McGuire, R. Stöhr, D. Xiao, *et al.*, “Direct visualization of magnetic domains and moiré magnetism in twisted 2D magnets,” *Science* **374**, 1140–1144 (2021).
- [199] F. Fabre, A. Finco, A. Purbawati, A. Hadj-Azzem, N. Rougemaille, J. Coraux, I. Philip, and V. Jacques, “Characterization of room-temperature in-plane magnetization in thin flakes of CrTe_2 with a single-spin magnetometer,” *Physical Review*

- Materials **5**, 034008 (2021).
- [200] H. Chen, S. Asif, M. Whalen, J. Támara-Isaza, B. Luetke, Y. Wang, X. Wang, M. Ayako, S. Lamsal, A. F. May, *et al.*, “Revealing room temperature ferromagnetism in exfoliated Fe₅GeTe₂ flakes with quantum magnetic imaging,” 2D Materials **9**, 025017 (2022).
 - [201] X.-Y. Zhang, Y.-X. Wang, T. A. Tartaglia, T. Ding, M. J. Gray, K. S. Burch, F. Tafti, and B. B. Zhou, “AC susceptometry of 2D van der Waals magnets enabled by the coherent control of quantum sensors,” PRX Quantum **2**, 030352 (2021).
 - [202] H. Heo, T. Kim, Y. Jeong, H. Park, and J. Jang, “Sagnac interferometer for time-resolved magneto-optical measurements,” Review of Scientific Instruments **93**, 013903 (2022).
 - [203] J. Hwang, D. Krylov, R. Elbertse, S. Yoon, T. Ahn, J. Oh, L. Fang, W.-j. Jang, F. H. Cho, A. J. Heinrich, *et al.*, “Development of a scanning tunneling microscope for variable temperature electron spin resonance,” Review of Scientific Instruments **93**, 093703 (2022).
 - [204] C. Klewe, Q. Li, M. Yang, A. T. N’Diaye, D. M. Burn, T. Hesjedal, A. I. Figueroa, C. Hwang, J. Li, R. J. Hicken, *et al.*, “Element-and time-resolved measurements of spin dynamics using X-ray detected ferromagnetic resonance,” Synchrotron Radiation News **33**, 12–19 (2020).
 - [205] A. Finco, A. Haykal, R. Tanos, F. Fabre, S. Chouaieb, W. Akhtar, I. Robert-Philip, W. Legrand, F. Ajejas, K. Bouzehouane, *et al.*, “Imaging non-collinear antiferromagnetic textures via single spin relaxometry,” Nature Communications **12**, 1–6 (2021).
 - [206] C. Du, T. Van der Sar, T. X. Zhou, P. Upadhyaya, F. Casola, H. Zhang, M. C. Onbasli, C. A. Ross, R. L. Walsworth, Y. Tserkovnyak, *et al.*, “Control and local measurement of the spin chemical potential in a magnetic insulator,” Science **357**, 195–198 (2017).
 - [207] B. Flebus and Y. Tserkovnyak, “Quantum-impurity relaxometry of magnetization dynamics,” Physical Review Letters **121**, 187204 (2018).
 - [208] P. Maletinsky, S. Hong, M. S. Grinolds, B. Hausmann, M. D. Lukin, R. L. Walsworth, M. Loncar, and A. Yacoby, “A robust scanning diamond sensor for nanoscale imaging with single nitrogen-vacancy centres,” Nature Nanotechnology **7**, 320–324 (2012).
 - [209] M. Pelliccione, A. Jenkins, P. Ovartchaiyapong, C. Reetz, E. Emmanouilidou, N. Ni, and A. C. Bleszynski Jayich, “Scanned probe imaging of nanoscale magnetism at cryogenic temperatures with a single-spin quantum sensor,” Nature Nanotechnology **11**, 700–705 (2016).
 - [210] H. Liu, D. Sun, C. Zhang, M. Groesbeck, R. Mclaughlin, and Z. V. Vardeny, “Observation of exceptional points in magnonic parity-time symmetry devices,” Science Advances **5**, eaax9144 (2019).
 - [211] S. Spielman, K. Fesler, C. Eom, T. Geballe, M. Fejer, and A. Kapitulnik, “Test for nonreciprocal circular birefringence in YBa₂Cu₃O₇ thin films as evidence for broken time-reversal symmetry,” Physical Review Letters **65**, 123 (1990).
 - [212] S. Spielman, J. Dodge, L. Lombardo, C. Eom, M. Fejer, T. Geballe, and A. Kapitulnik, “Measurement of the spontaneous polar Kerr effect in YBa₂Cu₃O₇ and Bi₂Sr₂CaCu₂O₈,” Physical Review Letters **68**, 3472 (1992).
 - [213] J. Xia, P. T. Beyersdorf, M. M. Fejer, and A. Kapitulnik, “Modified Sagnac interferometer for high-sensitivity magneto-optic measurements at cryogenic temperatures,” Applied Physics Letters **89**, 062508 (2006).
 - [214] J. Xia, Y. Maeno, P. T. Beyersdorf, M. Fejer, and A. Kapitulnik, “High resolution polar Kerr effect measurements of Sr₂RuO₄: Evidence for broken time-reversal symmetry in the superconducting state,” Physical Review Letters **97**, 167002 (2006).
 - [215] A. Fried, M. Fejer, and A. Kapitulnik, “A scanning, all-fiber Sagnac interferometer for high resolution magneto-optic measurements at 820 nm,” Review of Scientific Instruments **85**, 103707 (2014).
 - [216] X. Zhu, “Symmetry consideration in zero loop-area Sagnac interferometry at oblique incidence for detecting magneto-optic Kerr effects,” Review of Scientific Instruments **88**, 083112 (2017).
 - [217] X. Zhu, R. Ullah, and V. Taufour, “Oblique-incidence Sagnac interferometric scanning microscope for studying magneto-optic effects of materials at low temperatures,” Review of Scientific Instruments **92**, 043706 (2021).
 - [218] Z. Huang, B. P. Bloom, X. Ni, Z. N. Georgieva, M. Marciesky, E. Vetter, F. Liu, D. H. Waldeck, and D. Sun, “Magneto-optical detection of photoinduced magnetism via chirality-induced spin selectivity in 2D chiral hybrid organic–inorganic perovskites,” ACS Nano **14**, 10370–10375 (2020).
 - [219] S. Baumann, W. Paul, T. Choi, C. P. Lutz, A. Ardavan, and A. J. Heinrich, “Electron paramagnetic resonance of individual atoms on a surface,” Science **350**, 417–420 (2015).
 - [220] P. Willke, A. Singha, X. Zhang, T. Esat, C. P. Lutz, A. J. Heinrich, and T. Choi, “Tuning single-atom electron spin resonance in a vector magnetic field,” Nano Letters **19**, 8201–8206 (2019).
 - [221] M. Hervé, M. Peter, T. Balashov, and W. Wulfhkel, “Towards laterally resolved ferromagnetic resonance with spin-polarized scanning tunneling microscopy,” Nanomaterials **9**, 827 (2019).
 - [222] J. Goulon, A. Rogalev, F. Wilhelm, C. Goulon-Ginet, and G. Goujon, “Element-selective X-ray detected magnetic resonance: A novel application of synchrotron radiation,” Journal of Synchrotron Radiation **14**, 257–271 (2007).
 - [223] D. Arena, Y. Ding, E. Vescovo, S. Zohar, Y. Guan, and W. Bailey, “A compact apparatus for studies of element and phase-resolved ferromagnetic resonance,” Review of Scientific Instruments **80**, 083903 (2009).
 - [224] W. Bailey, C. Cheng, R. Knut, O. Karis, S. Auffret, S. Zohar, D. Keavney, P. Warnicke, J.-S. Lee, and D. Arena, “Detection of microwave phase variation in nanometre-scale magnetic heterostructures,” Nature Communications **4**, 1–6 (2013).
 - [225] G. van der Laan, “Time-resolved X-ray detected ferromagnetic resonance of spin currents,” Journal of Electron Spectroscopy and Related Phenomena **220**, 137–146 (2017).